Posted on 9 Mar 2023 — The copyright holder is the author/funder. All rights reserved. No reuse without permission. — https://doi.org/10.22541/essoar.167839709.98981541/v1 — This a preprint and has not been peer reviewed. Data may be preliminary.

Peng Feng[1], Rüdiger Haas[1], and Gunnar Elgered[1]

[1]Department of Space, Earth and Environment, Chalmers University of Technology, Onsala Space Observatory

March 9, 2023

A new tropospheric error model for ground-based GNSS interferometric reflectometry: theory and validation

Peng Feng[a], Rüdiger Haas[a], Gunnar Elgered[a]

[a]*Department of Space, Earth and Environment, Chalmers University of Technology, Onsala Space Observatory, Onsala, SE-439 92, Sweden*

Abstract

We deduce a new tropospheric error model for ground-based GNSS interferometric reflectometry (GNSS-IR), the NITE (New Interferometric Tropospheric Error) model. This model contains two parts, a straight-line geometric error and a path delay. The geometric error uses specular reflection, taking into account the atmospheric bending and the earth curvature effects. The path delay follows the definition of the mapping function. We validate the NITE model together with two previously used models, the bending correction and the mapping function path delay (MPF delay) using raytracing and radiosonde data. The raytracing results show that the newly-developed NITE model is more accurate than the previous models. Numerically, for a GNSS antenna with a 20 m height difference to the sea level, the geometric tropospheric error is < 5 % of the path delay error. We further investigate and compare six tropospheric error correction strategies for GNSS-IR sea level monitoring using two sets of experiments. With an elevation angle range test using GNSS stations with large height differences to the sea level, we show that applying no troposphere error corrections and applying the bending correction plus the MPF delay both introduce large elevation-dependent biases. Analyzing time series of differences between GNSS-IR derived sea level and corresponding results from co-located tide gauges, we show that the bending correction with the widely used Bennett equation introduces long-term (4 h to months) trends in the sea-level retrievals. This is eliminated by using the Ulich equation in the bending correction. In our experiment, the accuracy improvement due to the NITE model is not as clear as in the raytracing simulations. We identify one station where the NITE model produces better long-term ($\tau > 4$ h) stability. In others situations, the results from the NITE model have similar levels of random error. Finally,

we give a theoretical deduction showing that, except for extreme situations, both the bending correction and the MPF delay are approximations of the rigorous NITE model. Unlike what is previously regarded, the bending correction and the MPF delay are not complementary but equivalent at low elevation angles.

Keywords: GNSS-IR, tropospheric error, raytracing, sea level monitoring, earth curvature

1. Introduction

The application of Global Navigation Satellites Systems (GNSS) has been successfully extended from positioning, navigation and timing (PNT) (Dao et al., 2002; Pham, 2011) to environmental remote sensing. GNSS is today used, e.g., in meteorology (Duan et al., 2002), to study the atmosphere (Sokolovskiy et al., 2006), soil moisture (Larson et al., 2008; Larson, 2019), etc. GNSS reflectometry is one of these new applications which uses the reflected GNSS signal as a remote sensing tool to study the surrounding environment. For positioning, only the direct GNSS signals are useful while the reflected signals from nearby objects are regarded as an error source, referred to as the multipath error (Park et al., 2004). In GNSS reflectometry, by investigating the reflected signal and its interaction with the direct signal, we can measure snow depth and sea level, etc.

A typical GNSS-IR sea level monitoring setup is to install a GNSS antenna on the coast near the water, so that the antenna is receiving the combination of direct satellite signals and signals reflected off the ocean surface. The reflected signals travel a longer distance to reach the antenna than the direct ones. When a satellite ascends or descends, the phase lag between the reflected and direct signal will change and thus the power of the received signal at the antenna shows a periodic pattern. The power is recorded by GNSS receivers as signal-noise-ratio (SNR), thus this method is also referred to as the SNR-based GNSS-R. By determining the frequency of this varying SNR as a function of elevation angle we can derive the reflector height H_r from the GNSS antenna to the ocean surface. With a simplified (vacuum and planar reflection) geometry, the relationship between reflector height H_r and the reflected-versus-direct signal interferometric radio length τ_i can be written as (Georgiadou and Kleusberg, 1988; Larson et al., 2013b)

$$\tau_i = 2H_r \sin e_T \,, \tag{1}$$

where e_T is the true elevation angle of the satellite seen from the GNSS antenna.

GNSS-IR gives the height difference between the GNSS antenna and the sea surface. In combination with the inherent positioning ability of GNSS, GNSS-IR can provide sea level measurements (Larson et al., 2013a) with precision close to traditional tide gauges in a well-determined global terrestrial reference frame. This is called absolute sea level monitoring. The temporal resolution of GNSS-IR sea level results is also improving thanks to the development of multi-GNSS (Löfgren and Haas, 2014; Wang et al., 2019). However, systematic biases were found between GNSS-IR and traditional tide gauges (Geremia-Nievinski et al., 2020a; Strandberg, 2020), which impairs the advantage of the absolute sea level monitoring ability of GNSS-IR.

In this work, we focus on the tropospheric error for GNSS-IR. Due to the antenna design and physical surrounding limitations, GNSS-IR tends to use very low elevation angle observations, down to 2°. This makes the tropospheric error important. Several previous studies focused on the tropospheric error in GNSS reflectometry. Santamaría-Gómez and Watson (2017) studied the elevation-(angle)-dependent error on GNSS reflectometry and proposed to use an equation for astronomical refraction given by Bennett (1982) to correct the elevation angle. The Bennett 1982 equation is now widely used in GNSS-IR studies (Roesler and Larson, 2018). Williams and Nievinski (2017) studied the impact of tropospheric path delay on sea-level retrievals with a wide range of stations and found a scale error due to a lack of a proper troposphere delay correction. However, angular refraction was neglected in that work and the tropospheric delay was obtained directly using the mapping function products without further adaption. In previous studies (e.g., Treuhaft et al., 2001; Fabra et al., 2012; Williams and Nievinski, 2017), it is usually assumed that the path delay taken by the direct and reflected signals is equal from the satellite down to the height of the antenna. Nikolaidou et al. (2020) quantitatively studied the tropospheric error for GNSS-IR using 3D raytracing together with a standard atmosphere model, and claimed that the linear and angular refraction contributions to GNSS-IR have similar magnitude and they both evolve linearly with the reflector height and exponentially with satellite elevation angle.

However, the results from these previous investigations contradict each other. Santamaría-Gómez and Watson (2017) apply only the angular tropospheric bending correction, while Williams and Nievinski (2017) apply only the tropospheric path delay correction. These two corrections are differ-

ent and both authors claim that the elevation dependence is removed from the experiment results. On the other hand, the results by Nikolaidou et al. (2020) suggest that using only one of the corrections alone is not sufficient. In practice, some studies choose to correct both the bending and delay errors (e.g., Peng et al., 2019; Ye et al., 2022). Some studies choose to not apply tropospheric error correction at all (e.g., Roussel et al., 2015; Tabibi et al., 2020; Geremia-Nievinski et al., 2020a; Wang et al., 2021a,b; Gravalon et al., 2022), and some study chooses to apply only one of them (e.g., Xie, 2022; Wang et al., 2022).

In the following we investigate the tropospheric geometric error and path delay error in GNSS-IR sea level monitoring. In Section 2 we give the deduction of analytical equations for the troposphere geometric and path delay suitable for GNSS-IR, with a focus on sea leveling monitoring. In Section 3, the sub-component and total tropospheric error are validated using raytracing with radiosonde data. In Section 4 we present experimental assessment results of tropospheric error models using stations with different reflector heights. Section 5 discusses the relationship between the new GNSS-IR tropospheric model and the previous ones. In Section 6 we summarize this work and discuss the limitations of this new GNSS-IR tropospheric error model.

2. GNSS-IR tropospheric error model

2.1. Geometric interferometric tropospheric error

Figure 1 depicts the geometry of the GNSS-IR, considering atmospheric refraction and the earth surface curvature. The space between the ocean surface to the satellite is divided into 3 layers. The 1st layer starts from the sea surface and ends at the GNSS antenna. Since we limit the model to ground-based GNSS-IR, the 1st layer has a thickness of < 100 m. The 2nd layer begins at the GNSS antenna and ends at the top of the atmosphere, which is ≈ 100 km (Fleming et al., 1990). The area from the top of the atmosphere to the satellite, which is $> 20,000$ km, is described by the 3rd layer. The large difference in magnitude allows us to apply some approximations without losing much accuracy.

We first look at the direct signal path. Due to the atmospheric refraction, the true signal path is curved, instead of a straight line. The major part of the bending occurs in the 2nd layer, as the 1st layer is a lot smaller and the 3rd layer is almost vacuum. We start our deduction by first introducing the atmospheric bending angle. The bending angle is the angular difference

between the apparent elevation angle e_A and true elevation angle e_T for the direct signal path:

$$\Delta e = e_A - e_T \tag{2}$$

This bending angle is well studied in astronomy since angular observables are widely used in optical astronomy (Saastamoinen, 1973; Stone, 1996). Santamaría-Gómez and Watson (2017) studied this bending angular error on GNSS reflectometry and adopted an equation given by Bennett (1982)

$$\Delta e = \frac{510}{\frac{9}{5}T + 492} \frac{P}{1010.16} \cot(e_T + \frac{7.31}{e_T + 4.4}) , \tag{3}$$

where T is the temperature in ℃, P the pressure in hPa at the GNSS antenna and e_T is the true elevation angle. Notice that Equation (3) does not require the input of water vapor pressure, because the impact of water vapor at optical wavelength is small (Boisits et al., 2020). However, tropospheric water vapor is a major error contributor to GNSS signal propagation (e.g., Niell, 1996; Landskron and Böhm, 2018), and the basis of GNSS meteorology (e.g., Bevis et al., 1992; Elgered et al., 1997). For radio frequencies, studies show that the bending angle is proportional to the ground refractivity index (Meeks, 1976; Stone, 1996). Together with the elevation angle dependence, a model for radio telescope pointing error correction given by Ulich (1981) is

$$\Delta e = 10^{-6} N_0 \frac{\cos e_T}{\sin e_T + 0.00175 \tan(87.5^\circ - e_T)} , \tag{4}$$

where N_0 is the ground refractivity. The refractivity $N = 10^6(n-1)$ and n is the frequency-dependent atmospheric refractive index. N and n are physically equivalent. We will refer to N as refractivity and n as refractive index. For GNSS, the latest development of atmosphere refractivity is given by Rüeger (2002):

$$N_0 = K_1 \frac{P_d}{T} + K_2 \frac{P_w}{T} + K_3 \frac{P_w}{T^2} \tag{5}$$

Here, P_d is the dry pressure and P_w is the water vapor pressure, both in hPa, and T is the temperature in kelvin. The constant coefficients are $K_1 =$ 77.6890 (K/hPa), $K_2 =$ 71.2952 (K/hPa), and $K_3 =$ 375463 (K^2/hPa), respectively. We will always use the Ulich equation (Eq. (4)) to calculate the bending angle in the following deductions, except for the experiment part where we include the Bennett equation for comparison.

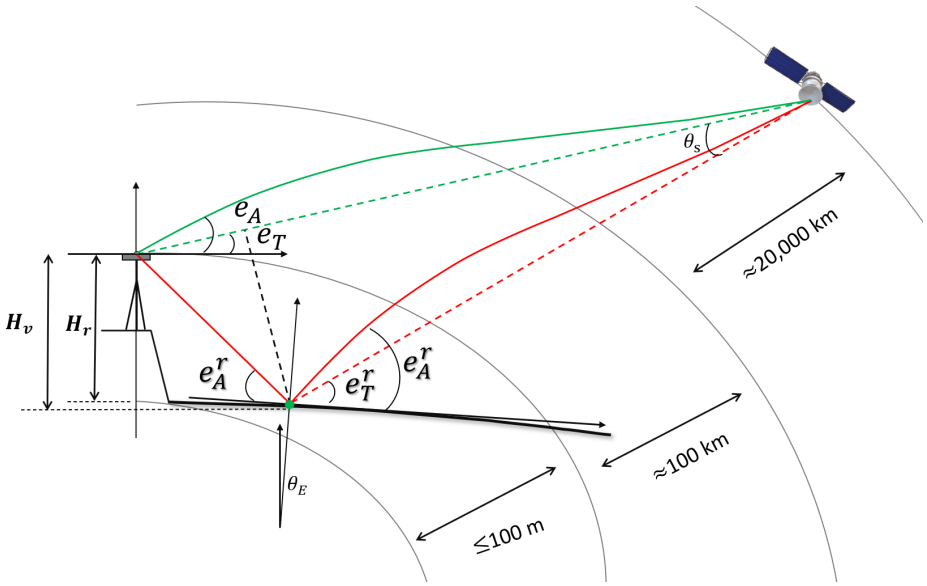

Figure 1: Geometry of coastal GNSS-IR with atmospheric refraction and earth curvature (not to scale).

We then look at the reflected signal path. The reflected signal path can be divided at the reflection point into a down-leg and an up-leg part. The down-leg denotes the signal from the satellite to the reflection point. The up-leg denotes the signal from the reflection point to the GNSS antenna. The true elevation angle e_T^r and the apparent elevation angle e_A^r of the reflected down-leg signal are slightly different from that of the direct signal. This is due to the finite distance of the satellite and the earth curvature. The finite distance of the satellite means that the direct and reflected signal form a small angle, marked as θ_S in Fig. 1. The earth center angle from the reflection point to the antenna is marked as θ_E. As shown in Table 1, these two angles are about 2 orders of magnitude smaller than Δe and 4 orders smaller than e_T. We can derive approximate expressions for θ_E and θ_S as

$$\begin{cases} \theta_E = \dfrac{H_r}{R \tan e_A} \\ \theta_S = \dfrac{2H_r \cos e_T}{L} \end{cases}, \tag{6}$$

where R is the mean radius of the earth. The unit of θ_E and θ_S are radian and L is the geometrical distance from the antenna to the satellite. Some studies

showed that the impact of a finite satellite distance on signal propagation is small for GNSS (Zus et al., 2015). Comparing θ_E and θ_S, the former is significantly larger, especially at low elevation angles (see Table 1). By including θ_S, the reflected and the direct signal will actually intersect at the satellite. Then the interferometric radio length can be clearly and precisely defined. If θ_S is ignored, i.e. the reflected and direct signal are parallel to each other, one will have to find a starting point to calculate the interferometric radio length. The choice of starting point can introduce an uncertainty. For GNSS satellites, the orbit radius is about 26,000 km thus L is about 23,700 km ($e_T = 20°$) to 25,600 km ($e_T = 2°$). The angle θ_E is 22 times the angle θ_S at 5°, and 49 times of θ_S at 2°. We keep the angle θ_S for completeness but we will use a rough approximation as $L \approx 4R$ for current GNSS satellites.

Table 1: Magnitude of true elevation angle e_T, apparent elevation angle e_A, earth center angle θ_E and satellite angle θ_S, for different reflector heights H_r, with $N_0 = 320$ ppm.

	e_T (e_A)							
	2°(2.30°)		3°(3.24°)		5°(5.17°)		10°(10.09°)	
H_r (m)	θ_E	θ_S	θ_E	θ_S	θ_E	θ_S	θ_E	θ_S
10	$2.2e^{-3}$	$4.5e^{-5}$	$1.5e^{-3}$	$4.5e^{-5}$	$9.9e^{-4}$	$4.5e^{-5}$	$5.0e^{-4}$	$4.4e^{-5}$
20	$4.5e^{-3}$	$9.0e^{-5}$	$3.2e^{-3}$	$9.0e^{-5}$	$2.0e^{-3}$	$8.9e^{-5}$	$1.0e^{-3}$	$8.8e^{-5}$
40	$8.9e^{-3}$	$1.8e^{-4}$	$6.3e^{-3}$	$1.8e^{-4}$	$4.0e^{-3}$	$1.8e^{-4}$	$2.0e^{-3}$	$1.8e^{-4}$
60	$1.3e^{-2}$	$2.7e^{-4}$	$9.5e^{-3}$	$2.7e^{-4}$	$6.0e^{-3}$	$2.7e^{-4}$	$3.0e^{-3}$	$2.7e^{-4}$
100	$2.2e^{-2}$	$4.5e^{-4}$	$1.6e^{-2}$	$4.5e^{-4}$	$9.9e^{-3}$	$4.5e^{-4}$	$5.0e^{-3}$	$4.4e^{-4}$

The true elevation angle e_T^r and the apparent elevation angle e_A^r of the reflected signal down-leg are:

$$\begin{cases} e_T^r = e_T + \theta_E + \theta_S \\ e_A^r \approx e_A + \theta_E + \theta_S \end{cases} \tag{7}$$

Except for the rotation of the local vertical expressed by θ_E, the earth curvature has a more direct effect. The reflection point is slightly lower than that of the "plane reflection" (Kwok, 2017). We define a vertical height H_v as the vertical distance between the reflection point and the antenna in the

local earth center coordinate of the antenna (see Fig. 1):

$$H_v = H_r + R(1 - \cos\theta_E) \approx H_r + \frac{H_r^2}{2R\tan^2 e_A} \tag{8}$$

In Table 2 we list the approximate value of the effect $(H_v - H_r)$ caused by the earth curvature. This reflection point vertical displacement is about 1 cm for $H_r = 20$ m, $e_T = 3^\circ$, and close to 0.5 m for $H_r = 100$ m, $e_T = 2^\circ$.

Table 2: Reflection point vertical displacement $(H_v - H_r)$ in cm, $N_0 = 320$ ppm.

H_r (m)	2°	3°	5°	7°	10°	20°	30°	80°
10	0.5	0.2	0.1	<0.1	<01	<01	<0.1	<0.1
20	1.9	1.0	0.4	0.2	0.1	<0.1	<0.1	<0.1
40	7.8	3.9	1.5	0.8	0.4	0.1	<0.1	<0.1
60	17.5	8.8	3.5	1.8	0.9	0.2	0.1	<0.1
100	48.6	24.4	9.6	5.0	2.5	0.6	0.2	<0.1

The up-leg, which is the signal path from the reflection point to the GNSS antenna, is treated as a straight line with length:

$$L_{up} = \frac{H_v}{\sin(e_A^r + \theta_E)} \tag{9}$$

We can now write the interferometric radio length for GNSS-IR as:

$$\tau_i = H_v \frac{1 - \cos(e_T + e_A^r + \theta_E)}{\sin(e_A^r + \theta_E)} + (S_r - G_r) - (S - G) \tag{10}$$

The first term in Eq. (10) is obtained in the triangle formed by the satellite, the antenna, and the reflection point. The difference between Eq. (10) and Eq. (1) is the geometric tropospheric error of the NITE model.

When the reflection point is close, its vertical displacement can be neglected. For example, for $H_r = 10$ m and $e_T = 2^\circ$, $\frac{H_r^2}{2R\tan^2 e_A} \approx 5$ mm. Then Eq. (10) will thus simplify to:

$$\tau_i = H_r \frac{1 - \cos(e_T + e_A^r + \theta_E)}{\sin(e_A^r + \theta_E)} + (S_r - G_r) - (S - G) \tag{11}$$

When the true elevation angle is large, the atmospheric bending angle Δe will be small thus we have $e_A \approx e_T$ and $\theta_E \approx 0$, and Eq. (10) will simplify to:

$$\tau_i = 2H_v \sin e_T + (S_r - G_r) - (S - G) \tag{12}$$

When the antenna is close to the sea surface and the satellite elevation angle is large, Eq. (10) becomes Eq. (1), adding an interferometric curve path error. In Eq. (10), $(S - G)$ and $(S_r - G_r)$ are the differential length between the straight line and the true curved propagation path, for the direct and reflected down-leg signal, respectively. The curve path error can not be obtained without knowing the refractivity distribution along the signal path. Fortunately, this curve path effect is identical in GNSS positioning and is included in the generation of mapping functions (Möller and Landskron, 2019). In the next section when we derive the interferometric tropospheric path delay, this term will be covered.

2.2. Interferometric tropospheric path error

The radio signal is retarded due to the atmosphere refractivity and this is usually referred to as the tropospheric delay in GNSS positioning. The tropospheric delay is an important error source of GNSS and has been well-studied in positioning applications. Thanks to the developments of numerical weather models and high-performance computing, we now have state-of-art mapping function products available for correcting tropospheric errors (Lagler et al., 2013; Landskron and Böhm, 2018). With the predetermined value of mapping functions and the ever-growing navigation constellations, GNSS can estimate the troposphere-related zenith total delay (ZTD) and delay gradient parameters and they in return contribute to environmental remote sensing. We will use the mapping function developed for GNSS positioning and we will also use the upper atmosphere information (ZTD) obtained by the GNSS meteorology method to deduce the tropospheric path delay for GNSS-IR.

We start the modeling of the path delay by first defining the interferometric tropospheric path delay of GNSS-IR. The interferometric path delay is the difference between the tropospheric delay experienced by the reflected and direct GNSS signal,

$$D_i = D_r - D_d \,, \tag{13}$$

where D_i, D_r, and D_d, represent the interferometric, reflected and direct tropospheric delay, respectively. The direct signal path delay caused by the atmosphere is identical to that in GNSS positioning. According to the definition

$$D_d = \int_{ant}^{sat} (n(s) - 1)ds + (S - G)\,, \tag{14}$$

where $n(s)$ is the refraction index along the curved signal path, and $(S - G)$ is the differential length between the straight line and the true curved signal path, identical to the definition in Eq. (10). Eq. (14) can be used to calculate accurate tropospheric delay via a raytracing method and generate mapping functions. While in GNSS data processing, the tropospheric delay is then modeled as (Herring et al., 2010; Dach et al., 2015):

$$D_d = ZTD \cdot mpf(e_T) \tag{15}$$

Here, ZTD is the zenith total delay and $mpf(e_T)$ is the elevation angle dependent total mapping function.

Similar to the previous section, we consider the path delay separately for the down-leg and the up-leg for the reflected signal. The up-leg path is relatively small and the length is given in Eq. (9). Then we define an average layer refractivity N_l, expressed in ppm (parts per million), which is representative for the layer of atmosphere between the GNSS antenna to the reflecting surface. For a not-so-high antenna (a few meters above sea surface), we can simply use the refractivity at the antenna as the average layer refractivity. For an antenna that is located at 10 m above the sea surface, and assuming 300 ppm refractivity at the antenna, the refractivity at the reflection surface is about 300.375 ppm with an exponential vertical distribution. Besides, due to wind and atmospheric turbulence, in a layer of about 10 m above the sea surface, it is more reasonable to assume a well-mixed refractivity than an exponential decaying distribution. However, if the antenna is located high enough ($\sim$ 100 m), it is better to use the mean refractivity, taking into account the vertical distribution as,

$$N_l = N_0 \frac{1 + e^{\frac{H_r}{8000}}}{2}\,, \tag{16}$$

where N_0 is the refractivity measured at the GNSS antenna. Eq. (16) simply gives the average refractivity of the antenna and the reflecting surface with

a fixed scale height of 8000 m, assuming a linear vertical distribution in the small layer. Another choice would be averaging over integration, assuming an exponential refractivity profile. For an antenna that is 100 m above the sea surface, these two approaches differ by less than 0.004 ppm. The tropospheric delay of the reflected signal up-leg can be expressed by multiplying Eq. (16) and Eq. (9):

$$D_{up} = 10^{-6} N_l \frac{H_v}{sin(e_A^r + \theta_E)} \tag{17}$$

The tropospheric path delay of the reflected signal down-leg is evaluated using the definition of the mapping function

$$D_{down} = (ZTD + ZTD_l) \cdot mpf(e_T^r)\,, \tag{18}$$

where ZTD_l is the "layer ZTD" between the GNSS antenna and the reflector surface as $ZTD_l = 10^{-6} N_l H_r$. Comparing Eq. (18) and Eq. (15), they are both applying the definition of the mapping function. The mapping function value for the reflected down-leg signal is close to but not the same as that of the direct signal. This is because of two reasons. Firstly, the mapping function is a function of station height. Secondly, the true elevation angles are not identical, i.e., $e_T^r \neq e_T$. A height correction is needed for sites at different altitudes when applying the mapping function (Yan et al., 2002; Zus et al., 2015). A height correction for the hydrostatic mapping function is given by Niell (1996) as

$$\frac{\partial mpf}{\partial h} = \frac{1}{sine_T} - \frac{1 + \frac{a}{1+\frac{b}{1+c}}}{sine_T + \frac{a}{sine_T + \frac{b}{sine_T + c}}}\,, \tag{19}$$

where $a = 0.0000253$, $b = 0.00549$, $c = 0.00114$. The accuracy of the mapping function height correction given by Eq. (19) has been questioned (Yan et al., 2002; Zus et al., 2015). It is still the only available model for mapping function height correction (Landskron, 2017). A more accurate height correction can be realized by numerical methods, which means using raytracing to obtain mapping function at multiple altitudes at a global scale, with a fine enough numerical weather model. That is out of the scope of this work and a numerical weather model with a vertical resolution of about 10 m level is currently not available. As we limit our model for ground-based GNSS reflectometry applications with a maximum reflector height of 100 m, numerical

results show that the height correction term is secondary compared to the effects of the true elevation angle difference.

The difference between the true elevation angle of the direct and reflected down-leg signal is given by Eq. (7). The mapping function is usually expressed as a parameterized continued fraction. The derivative of the mapping function can be analytically expressed as

$$\frac{\partial mpf}{\partial e_T} = \left(\frac{a(\cos e_T - \frac{b\cos e_T}{(c+\sin e_T)^2})}{(\frac{b}{c+\sin e_T} + \sin e_T)^2} - \cos e_T \right) \cdot mpf(e_T)\,, \tag{20}$$

with a, b and c being the mapping function products (Landskron, 2017). Eq. (20) is complicated in form but the meaning is straightforward. It gives the partial derivative of the mapping function with respect to the true elevation angle. In practice, this partial derivative can also be numerically calculated by first calculating the mapping function at two slightly different elevation angles. An implementation of Eq. (20) is included in the code to use the GMF product available (see re3data.org). Now Eq. (18) can be written as:

$$D_{down} = (ZTD + ZTD_l) \cdot \left[mpf(e_T) - (\frac{\partial mpf}{\partial e_T}\Delta e_T + \frac{\partial mpf}{\partial h} H_r) \right] \tag{21}$$

Considering that ZTD_l is small compared to ZTD (for an antenna of 100 m distance to the sea surface, $ZTD_l \approx \frac{ZTD}{80}$) and the same situation stands for the mapping function and its differences. Combining Eqs. (17) and (21) and substitute the direct signal tropospheric delay by Eq. (15), the interferometric tropospheric path delay of GNSS-IR is:

$$D_i = \frac{10^{-6} N_l H_v}{\sin{(e_A^r + \theta_E)}} + ZTD_l mpf(e_T) - ZTD \left(\frac{\partial mpf}{\partial e_T}\Delta e_T + \frac{\partial mpf}{\partial h} H_r \right) \tag{22}$$

Eq. (22) gives the interferometric tropospheric path delay of GNSS-IR as a function of the reflector height $H_r(H_v)$, the average layer refractivity N_l, the true elevation angle e_T, the zenith total delay ZTD, the mapping function, and the derivative of the mapping function. While Eq. (22) is complicated the only required observable data is the refractivity at the antenna, i.e., meteorology data. ZTD can be estimated from the GNSS data processing and all the partial derivatives of the mapping function are contained in the mapping function products. Eq. (22) is the interferometric path delay of the NITE model.

While Eq. (22) gives the interferometric tropospheric path delay in the form of forward modeling, it is challenging to directly apply it, especially for the SNR-based GNSS-IR. The problem is that the earth curvature effect given by Eq. (8) is dependent on reflector height H_r and has an ${H_r}^2$ term. We adopt a simple first-order correction by introducing an H_v to H_r ratio K expressed as

$$K = \frac{H_v}{H_r} \approx 1 + \frac{H_r^0}{2R\tan^2 e_A}\,, \tag{23}$$

where H_r^0 is a prior value of H_r. This a priori value H_r^0 does not need to be known very accurately for normal ground-based GNSS-IR. Or it can be solved iteratively if H_r changes dramatically (Semmling et al., 2012). Combining Eqs. (10) and (22) and inserting K, we can extract the relative reflector height H_r term, to obtain an equation suitable to be applied to Eq. (1) directly at the observable level using a variable substitute method (Strandberg, 2020) as:

$$\begin{aligned}\tau_i = H_r\Bigg[K\frac{1-\cos(e_T+e_A^r+\theta_E)}{\sin(e_A^r+\theta_E)} + K\frac{10^{-6}N_l}{\sin(e_A^r+\theta_E)} \\ + 10^{-6}N_l mpf(e_T) - ZTD(\frac{\partial mpf}{\partial e_T}\frac{1}{R\tan e_A} + \frac{\partial mpf}{\partial h})\Bigg]\end{aligned} \tag{24}$$

3. Raytracing Validation

3.1. Validating sub-components of the tropospheric error

In this section, we validate the two sub-components of the GNSS-IR tropospheric error using raytracing. Due to the existence of the atmosphere, (a) the position of the reflection point is changed, (b) the GNSS signal propagates along a curved path and (c) the signal speed is slower. Theoretically, the first two effects are combined to form the interferometric geometric tropospheric error, and the third effect is defined as the interferometric tropospheric path delay. In practice, the mapping function products for GNSS positioning are used to calculate the path delay, thus the curve path effects are included. In Section 2.1 we only modeled the effects of the reflection point change, which is the straight-line part of the interferometric tropospheric geometric error. And in Section 2.2 we gave the expression for interferometric tropospheric path delay, with the curve path effects included.

We use raytracing to validate the tropospheric straight-line geometric error and the path delay from the NITE model. The 2-step 2D raytracing

method for GNSS-IR is documented in Appendix A. This raytracing algorithm considers the curvature of the earth and the finite distance of GNSS satellites. We use the refractivity profile from radiosonde observations (Durre et al., 2006) as input for the raytracing. In the upper part of the atmosphere, above the troposphere where radiosonde data is not available, we extend the profile to 100 km with the standard atmosphere model (Minzner et al., 1976). In total 14 globally distributed radiosonde stations were chosen following previous GNSS-IR studies (Geremia-Nievinski et al., 2020b), but also to cover a wide range of climate regions like Antarctica (Xie, 2022). The radiosondes profiles are used as realistic samples to evaluate the consistency between the NITE model and numerical raytracing. Information of radiosonde stations together with the 4-digit name of nearby GNSS stations are presented in Table 3.

Table 3: Radiosonde stations for raytracing validation.

Radiosonde station	Latitude (°)	Longitude (°)	Height (m)	Nearby GNSS station
FPM00091938	−17.5550	−149.6200	2.0	FAA1
ASM00094672	−34.9525	138.5203	6.1	SPRB
GRM00016754	35.3353	25.1819	35.0	NOMI
USM00072327	36.2472	−86.5631	180.2	KYDH
USM00072469	39.7675	−104.8694	1611.0	P041
ASM00094975	−42.8339	147.5033	4.0	BUR2
SPM00008023	43.4911	−3.8006	52.0	SCOA
USM00072797	47.9339	−124.5603	56.8	SC02
FRM00007110	48.4442	−4.4119	99.0	BRST
SWM00002527	57.6572	12.2911	164.0	OSOU
USM00070326	58.6811	−156.6514	8.4	PBAY
AYM00089571	−68.5740	77.9672	18.0	DAV1
AYM00089532	−69.0050	39.5811	18.4	SYOG
SVM00001004	78.9233	11.9222	15.5	NYA2

The interferometric radio length assuming a vacuum, plane reflection is given by Eq. (1). We will use Eq. (1) as a base value and refer to it as the $\sin e_T$ model. Eq. (10) (NITE geometric model) differs from Eq. (1) as we took the troposphere bending effect and the earth curvature into account. The difference between Eq. (10) and Eq. (1) is the straight-line tropospheric geometric error. In Fig. 2, the straight-line tropospheric geometric error from

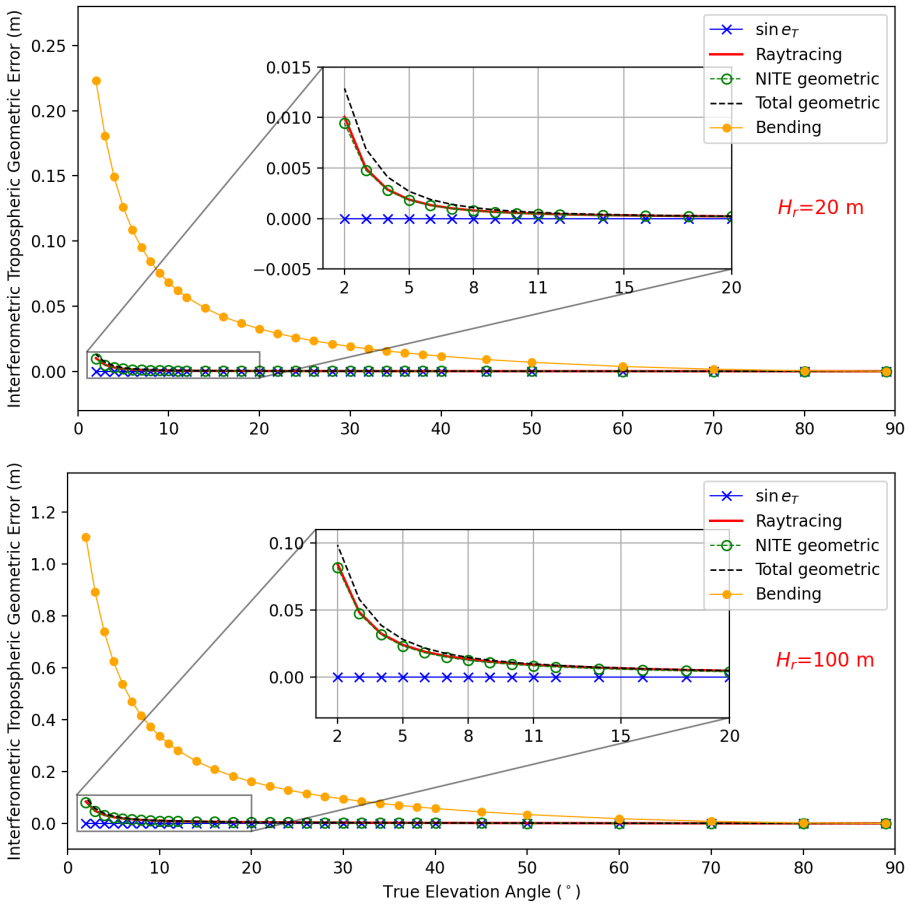

Figure 2: Straight-line interferometric tropospheric geometric error compared to raytracing (zoom in part). The vacuum τ_i ($\sin e_T$) was subtracted. The results are presented for two reflector heights $H_r = 20$ m (top) and $H_r = 100$ m (bottom), with a refractivity of 320 ppm at the antenna. The black dashed line shows the tropospheric geometric error with curve path effects included.

Eq. (10) is compared to raytracing values. The $\sin e_T$ model was used as the base and subtracted so its values are shown as zero in Fig. 2. Results for reflector heights of 20 m and 100 m are presented and the ground refractivity was chosen to be 320 ppm (average summer condition in Gothenburg, Sweden). The NITE geometric model gives a good estimation of the straight-line tropospheric geometric error. For an antenna at 20 m height above the sea surface, at 2° elevation, the straight-line tropospheric geometric error from

raytracing is ≈ 1 cm. The NITE geometric model given by Eq. (10) differs from raytracing at the level of < 1 mm. For a reflector height $H_r = 100$ m and $e_T = 2°$, the straight-line tropospheric geometric error from raytracing is ≈ 8 cm and the NITE geometric model has an error of ≈ 3 mm. The error of the NITE geometric model increases when the relative reflector height increases or when the elevation decreases. The total interferometric tropospheric geometric error, with the curve path effects included, is plotted in Fig. 2 with a black dashed line. The curve path affects is about 3 mm ($H_r = 20$ m, $e_T = 2°$) to 1 cm ($H_r = 100$ m, $e_T = 2°$). The fact that the $\sin e_T$ model and raytracing only have differences of about 1 cm for $H_r = 20$ m, $e_T = 2°$ means the interferometric tropospheric geometric error is very small.

The geometric interferometric tropospheric error given by Eq. (10) might be confused with the "bending correction" used in Santamaría-Gómez and Watson (2017), as they both use the input of the apparent elevation angle. However, they are very different both in physical meaning and in magnitude. With the "bending correction", the true elevation angle in Eq. (1) was replaced by the apparent elevation angle as:

$$\tau_i = 2H_r \sin e_A \tag{25}$$

Thus, the value of the bending correction is $\Delta\tau_i = 2H_r(\sin e_A - \sin e_T)$, which is also presented in Fig. 2 (orange line with solid dots). As we can see, the bending correction gives a much larger correction value. Even if the curve path effects are added, the bending correction will still not match the total interferometric tropospheric geometric error. The bending correction by Santamaría-Gómez and Watson (2017) is not modeling the geometric part of the tropospheric error.

On the other hand, the $\sin e_T$ model, which is based on a vacuum median, plane reflector propagation performs surprisingly well on calculating the interferometric radio length. However, the troposphere refraction does impact the signal path and thus causes an interferometric geometric tropospheric error. In Fig. 3, the straight-line interferometric radio length (not just troposphere) from raytracing and model values for $H_r = 20$ m, $e_T = 2°$ are plotted versus ground refractivity, using data from all the 14 sites. We can see from the raytracing results that the straight-line interferometric radio length does change with the ground refractivity, and that the NITE geometric model given by Eq. (10) fits the relation well. The $\sin e_T$ model however does not respond to ground refractivity variation. In our data set the ground

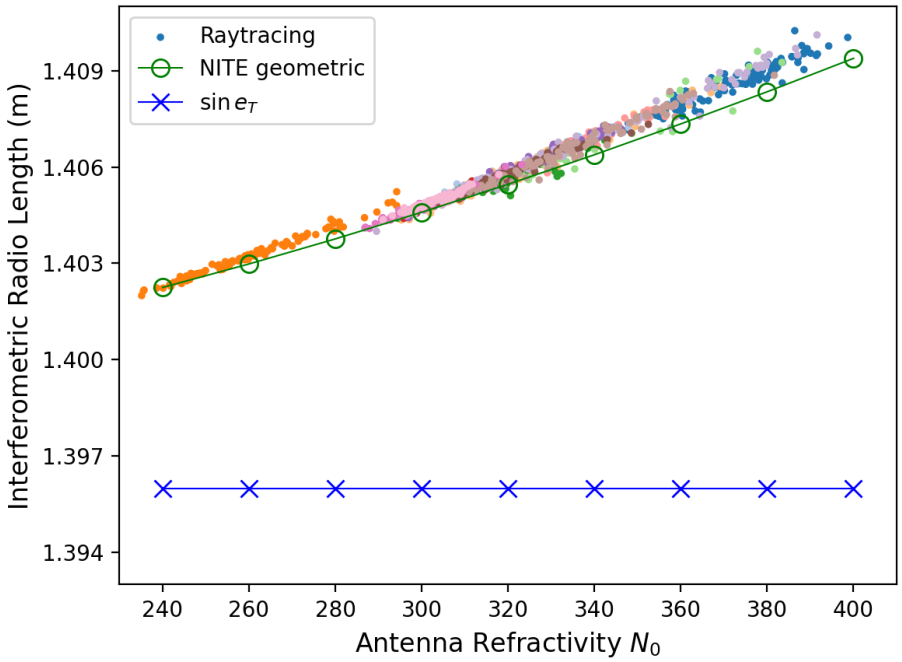

Figure 3: GNSS-IR straight-line geometric interferometric radio length (τ_i) versus GNSS antenna refractivity from raytracing (solid dots), the vacuum-based $\sin e_T$ model (blue crosses), and geometric part of the NITE model (green circles), for reflector height H_r = 20 m, elevation angle $e_T = 2°$. The plot uses radiosonde data from 14 globally distributed sites (in different colors).

refractivity ranges from 240 to 400 ppm, but ground refractivity for a specific location only covers part of this range. Using the $\sin e_T$ model to describe the interferometric radio length will introduce inhomogeneous errors for different locations.

For the interferometric tropospheric path delay, previously, some studies used a model to correct the tropospheric path delay directly using a mapping function (Williams and Nievinski, 2017) as the slant factor. This assumes that the path delays for the direct and reflected signal cancel out above the antenna and a mapping function is used to map the "layer ZTD" to different elevation angles. We will refer to it as the "MPF" delay model:

$$D_i = 2 \cdot 10^{-6} N_l H_r mpf(e_T) \tag{26}$$

However, the "cancels out above the antenna" assumption to some de-

gree contradicts the use of a mapping function as the slant factor, because a mapping function is determined for the whole atmosphere up to 80 km (Landskron and Böhm, 2018).

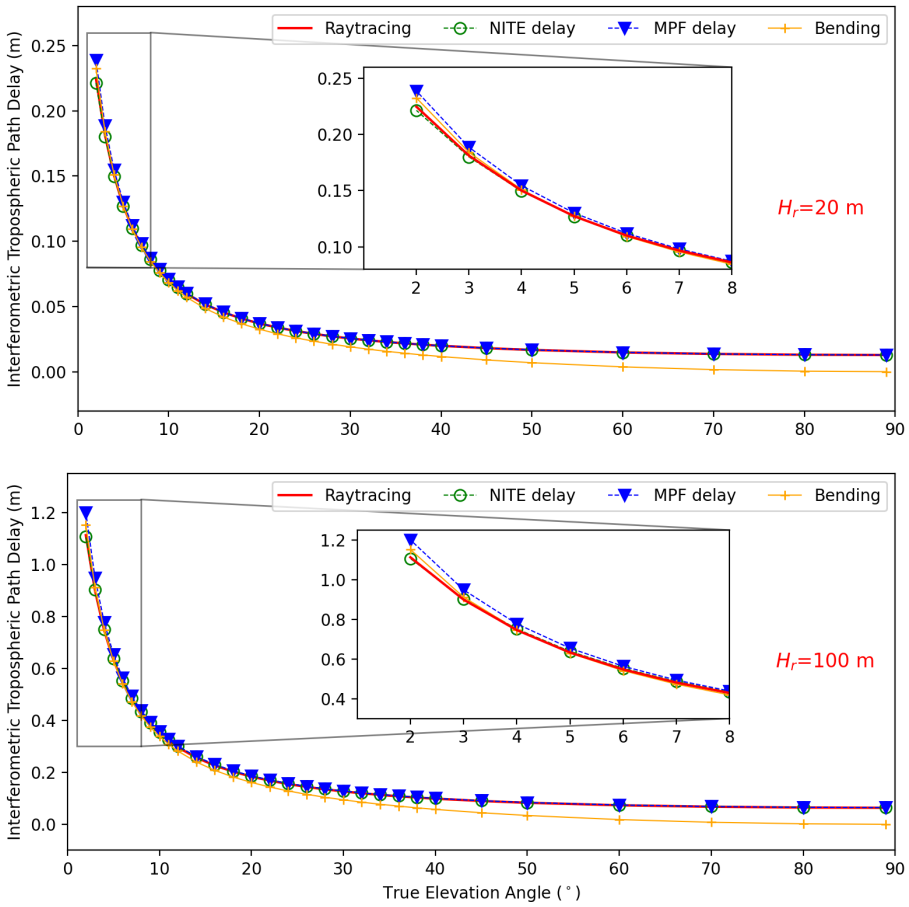

Figure 4: Interferometric tropospheric path delay from raytracing and different models using radiosonde refractivity profile with a ground refractivity of 320 ppm.

Fig. 4 depicts an example of interferometric tropospheric path delay over elevation angle from the MPF delay model, the NITE delay model, and the reference value from raytracing. The refractivity profile is derived from radiosonde data on a summer day in Landvetter Airport, Sweden, with a ground refractivity of 320 ppm. The bending correction is also plotted in Fig. 4. For the MPF and NITE delay models, we use the GMF mapping

function as input. For two reflector heights of 20 m (top) and 100 m (bottom), the NITE delay model (Eq. (22)) gives almost identical path delay as raytracing. The MPF model gives a slightly larger path delay than raytracing. For elevation angle $> 15^\circ$ the differences between the MPF and NITE model path delay and the raytracing are very small. The bending correction gives a correction that is overall very close to the interferometric tropospheric path delay. However, in the zenith direction, the apparent and true elevation angles are equal, which means no tropospheric correction with the bending correction at a high elevation angle. Comparing Fig. 4 and Fig. 2, it is clear that the path delay is the major part of the interferometric tropospheric error. For an antenna of 20 m height above the sea surface, the geometric part is < 5 % of the path delay at 2°, and at high elevation angles the geometric tropospheric error decreases to zero but not the path delay.

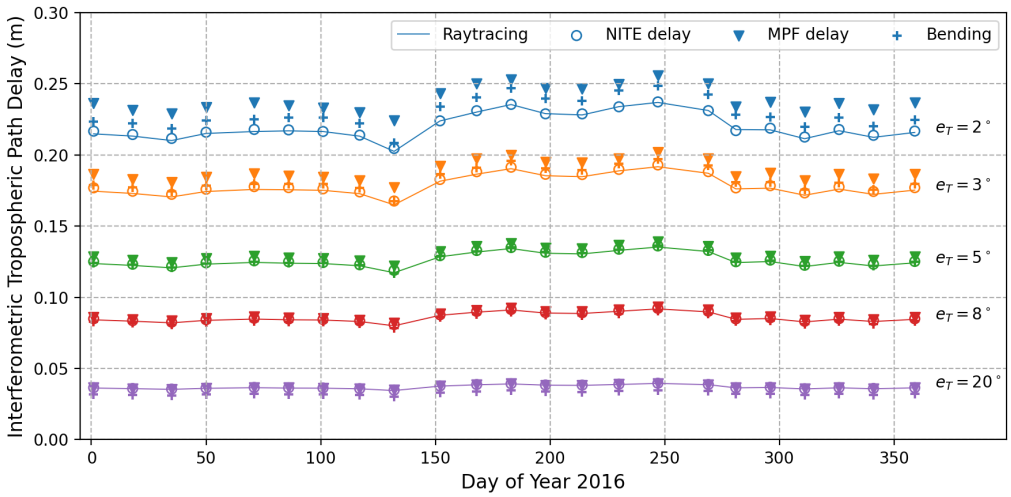

Figure 5: 1-year time series of tropospheric path delay of different models versus raytracing, with radiosonde refractivity profile from Landvetter Airport, Sweden, $H_r = 20$ m.

Fig. 5 gives 1-year long time series of GNSS-IR tropospheric path delay from the bending correction, the MPF and NITE model with $H_r = 20$ m, for $e_T = 2^\circ, 3^\circ, 5^\circ, 8^\circ, 20^\circ$. The NITE model gives the closest results to raytracing. The MPF model has a small positive bias over the year, though this radiosonde data comes from a place with an obvious seasonal phenomenon (southern Sweden). Interestingly, at 2° the bending correction seems to compensate for the tropospheric **path delay** better than the MPF delay model.

3.2. Total tropospheric error validation

Regardless of the definition of each sub-components, in practice, it is the total tropospheric error that impacts the observations. In this section, we validate the total tropospheric error given by the bending correction, the MPF delay model, and the NITE model. For the bending correction, the GNSS-IR interferometric radio length τ_i is given by Eq. (25). For the MPF model, the interferometric radio length is the sum of Eq. (1) and Eq. (26). For the NITE model, the interferometric radio length is the sum of Eq. (10) and Eq. (22).

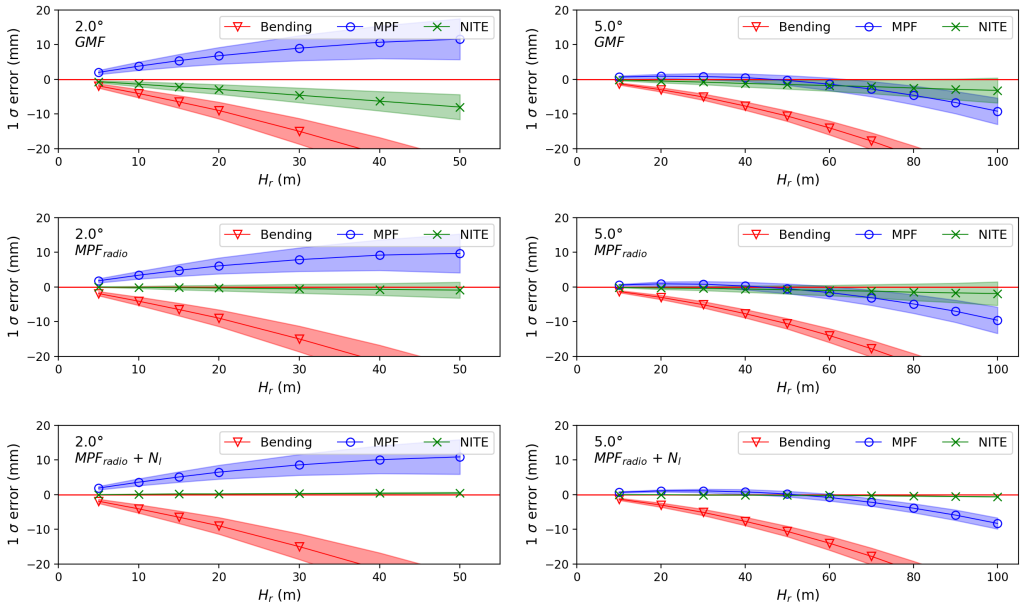

Figure 6: Tropospheric total delay model error at different reflector heights, for $e_T = 2°$ (left) and $e_T = 5°$ (right). Upper row, with GMF as model input. Middle row, with corresponding mapping function from radiosonde as input. Lower row, with corresponding mapping function and layer refractivity N_l from the radiosonde as input. Notice the different x-axis range for $e_T = 2°$ (left column) and $e_T = 5°$ (right column).

The total tropospheric error from the above three models was validated using raytracing. We used radiosonde balloon data as a realistic example of atmospheric profiles. One year of radiosonde data from 14 global stations (Table 3) was used in this simulation validation, but only two profiles were used for every 30 days. The average model errors for the three models are presented in Fig. 6. Detailed numerical values are given in Table 4. On the

left side of Fig. 6, the total tropospheric delay model errors are given for reflector height from 5 to 50 m for $e_T = 2^\circ$. The right side of Fig. 6 is for $e_T = 5^\circ$ and H_r from 10 to 100 m. In the upper row, the GMF (Boehm et al., 2006) and N_l from Eq. (16) were used as model input. The model bias with 1 σ standard deviation is plotted. We can see that the NITE model performs best, and the MPF model is next best. The MPF model tends to overestimate the tropospheric error while the bending correction underestimates the total tropospheric error. The NITE model also has smaller σ compared to the other two models, which means the NITE model is able to capture the variation of the total tropospheric error better, for different locations and times. For $e_T = 5^\circ$, both MPF and NITE models have very small errors compared to raytracing. The NITE model has a negative bias and the bias increases with H_r almost linearly (see Table 4).

Both the MPF and NITE models require the input of mapping function values and an average layer refractivity N_l. The accuracy of the mapping functions and N_l will impact their accuracy. In the middle row, the mapping function was generated from the corresponding radiosonde profile, i.e., an ideal mapping function. In the lower row in Fig. 6, both the mapping function and N_l are numerically obtained from the corresponding radiosonde profile. Comparing the middle and upper rows, we can see that the bias of the NITE model is almost removed with the "perfect" mapping function input, while the MPF model does not benefit much from the better mapping function values. Comparing the lower row and the middle row, we can see that the NITE model now gives nearly identical values as raytracing. This means the N_l given by Eq. (16) is the origin of random errors for the NITE model. These random errors increase with reflector height H_r. This is not surprising as Eq. (16) essentially solves the average layer refractivity below the GNSS antenna with only the refractivity at the antenna. In the lower rows, with the ideal N_l, the random errors (σ) of the MPF model are also reduced. The lower row of Fig. 6 shows that the NITE model has very good formal precision, but in practical applications, the NITE model will be limited by the accuracy of existing mapping function products and the representativeness of N_l.

The mapping function can be optimized at lower elevation angles for GNSS-IR application, considering that the GMF products are designed to be used for $e_T > 3^\circ$. We checked with 14 stations separately (not shown) and the bias of NITE model with GMF as input is very similar at all the stations though the weather conditions vary a lot. This is because the NITE model

Table 4: Tropospheric total delay model error in mm (bias and standard deviation) compare to raytracing, at different reflector heights H_r, for $e_T = 2^\circ$ and $e_T = 5^\circ$.

	$e_T = 2^\circ$				
Input	H_r	5 m	10 m	20 m	50 m
GMF	Bending	−1.9(0.6)	−4.1(1.2)	−9.0(2.4)	−29.1(6.0)
	MPF	+2.0(0.6)	+3.8(1.2)	+6.8(2.4)	+11.6(5.9)
	NITE	−0.7(0.3)	−1.4(0.7)	−2.9(1.4)	−8.0(3.6)
MPF_{radio}	Bending	−1.9(0.6)	−4.1(1.2)	−9.0(2.4)	**−29.1**(6.0)
	MPF	+1.8(0.6)	+3.4(1.1)	+6.1(2.3)	**+9.7**(5.6)
	NITE	<0.1(0.1)	−0.1(0.3)	−0.3(0.8)	**−0.9**(2.3)
MPF_{radio} N_l	Bending	−1.9(0.6)	−4.1(1.2)	−9.0(2.4)	−29.1(**6.0**)
	MPF	+1.9(0.5)	+3.6(1.0)	+6.5(2.0)	+10.9(**5.0**)
	NITE	<0.1(<0.1)	<0.1(<0.1)	+0.2(0.1)	+0.5(**0.2**)

	$e_T = 5^\circ$				
Input	H_r	10 m	20 m	50 m	100 m
GMF	Bending	−1.3(0.3)	−3.0(0.6)	−7.7(1.5)	−31.8(4.0)
	MPF	+0.7(0.3)	+0.9(0.6)	−0.3(1.4)	−9.2(3.8)
	NITE	−0.2(0.2)	−0.5(0.5)	−1.5(1.3)	−3.2(3.6)
MPF_{radio}	Bending	−1.3(0.3)	−3.0(0.6)	**−7.7**(1.5)	−31.8(4.0)
	MPF	+0.6(0.2)	+0.9(0.6)	**−0.5**(1.4)	−9.6(3.8)
	NITE	−0.1(0.1)	−0.3(0.4)	**−0.8**(1.2)	−1.9(3.4)
MPF_{radio} N_l	Bending	−1.3(0.3)	−3.0(0.6)	−7.7(**1.5**)	−31.8(4.0)
	MPF	+0.7(0.2)	+1.1(0.3)	+0.2(**0.8**)	−8.3(1.6)
	NITE	<0.1(<0.1)	<0.1(<0.1)	−0.2(<**0.1**)	−0.6(<0.1)

is sensitive to the derivative of the mapping function. The mapping function varies smoothly over time, location, and elevation angle. It is expected that the derivative of the mapping function will be smooth. However, it is difficult to have a much better equation than Eq. (16) for the average layer refractivity when H_r increases. The suggestion would be, for the sake of more accurate tropospheric error correction in GNSS-IR, that H_r should not be too large. The fact that uncertainty in N_l leads to the major part of random errors also suggests that there is a possibility to estimate the average layer refractivity

together with the sea level, similar to the estimation of GNSS ZTD and gradients (Davis et al., 1993).

4. Experimental Validation

In this section we test and compare the tropospheric error models discussed before with experiment data. We collected GNSS and meteorology data for 5 stations from DOY (day of year) 1, 2021 to DOY 180, 2022. The OSOU station with $H_r \approx 3.7$ m is located at Onsala Space Observatory, Sweden. The three stations SC02 ($H_r \approx 5.5$ m), AT01 ($H_r \approx 13$ m) and ELLY ($H_r \approx 33$ m) are all located in the USA. The NYA2 station is located in Norway with a reflector height of $H_r \approx 48$ m. These five stations have almost complete 1-Hz data records from the beginning of 2021 till the middle of 2022 and they also have usable SNR data for the GNSS-IR study with relatively large elevation angle coverage. We also obtained high temporal resolution (≈ 10 min) meteorology and tide gauge data for these five sites (see Section 6 for data availability). Unfortunately, we found no nearby tide gauge for AT01 with a good time resolution. We include AT01 because it has very good elevation angle coverage for GNSS-IR application and the first experiment does not require the use of tide gauge data. The SC02 has a similar reflector height as OSOU but a less usable elevation angle coverage. Thus SC02 was not used in the first experiment and AT01 was not used in the second experiment. Information about these five GNSS-IR sites is listed in Table 5.

We used the *gnssrefl* software by Roesler and Larson (2018) for data processing. For generating the true elevation angle, the GMB precise orbit products were used. We used 5 s SNR data for OSOU and SC02, 2 s SNR for

Table 5: Information for the five GNSS-IR stations.

Station (Country)	H_r (m)	Lat (°)	Long (°)	Azimuth mask (°)	Elevation Range Nodes (°)
OSOU(SWE)	3.7	57.393	11.914	70–260	2∼8∼15∼22.6∼32
SC02(USA)	5.5	48.546	-123.007	25–230	2∼7
AT01(USA)	13	63.484	-162.006	20–220	2∼5.4∼9∼13∼17
ELLY(USA)	33	33.583	-118.129	80–170 210–310	2∼4.2∼6.5∼8.7∼13
NYA2(NOR)	48	78.930	11.859	25–100	2∼4.2∼6.5∼8.7∼12

AT01, and 1 s SNR for ELLY and NYA2. The *gnssrefl* software currently only supports the bending correction with the Bennett 1982 equation. We turned off the tropospheric correction in the software. Instead, tropospheric error corrections were applied on the elevation angle of the SNR records using a variable substitute method (Strandberg, 2020). Except for the pressure, temperature and humidity data, the NITE model also takes the ZTD as input. The 5-minute ZTDs together with daily coordinates for the five stations were obtained using the Automatic Precise Positioning Service provided by Jet Propulsion Laboratory (JPL). The height-rate correction proposed by Larson et al. (2013b) was also applied. Fig. 7 gives the procedure of the GNSS-IR processing with the NITE tropospheric error correction.

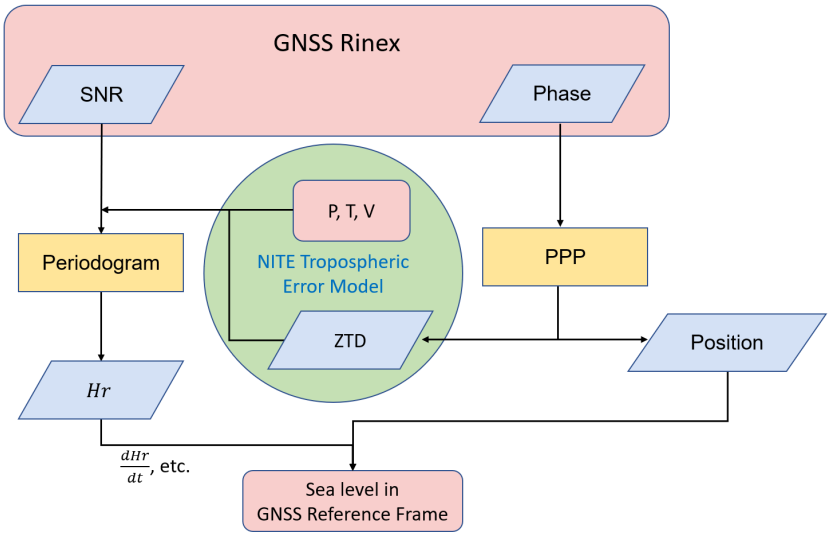

Figure 7: GNSS-IR sea level retrieval with the NITE tropospheric error correction.

We tested six tropospheric error correction strategies: (a) "Bending Bennett", applying the bending correction with the Bennett equation. (b) "MPF", applying only the path delay with the MPF model. (c) "Bending Ulich", applying the bending correction with the Ulich equation. (d) "NITE", applying the geometric and path delay model given by Eq. (10) and Eq. (22). (e) "No Troposphere", no tropospheric error correction was applied. (f) "Bending + MPF", applying the bending angle correction using the Ulich equation together with the path delay correction with the MPF model. GMF products were used when mapping function inputs were required.

4.1. Elevation Angle Range Test

Firstly, we did an elevation angle range test. We cut the SNR data into different elevation ranges. High-rate GNSS data were used to ensure that sufficient SNR samples were provided. The periodogram algorithm needs at least ≈ 3 cycles of data to stably retrieve the frequency. The elevation range cutting nodes were obtained individually for each station by dividing the elevation range between 2° to 30° into 2, 3, 4, 5, 6... average parts (sine value). Then we chose the elevation angle cut strategy that has the most nodes yet enough H_r solutions pass the quality check (Roesler and Larson, 2018). For example, for the OSOU station, we ran the GNSS-IR processing with elevation ranges of 2–8°, 8–15°, 15–22.6°, and 22.6–32°. The elevation angle cut strategy is listed in Table 5, together with the azimuth mask. This method is similar to the elevation angle truncate test in Ping et al. (1997) or the sliding window method used in Williams and Nievinski (2017). The difference is that here there is no overlap between elevation angle ranges so every solution is independent.

Fig. 8 gives a seven-day H_r time series of the elevation range cutting experiment for NYA2. H_r from all 4 elevation ranges varies in similar patterns, which confirms the effectiveness of this elevation cut strategy. An advantage of this elevation range cutting is that in stations where elevation angle coverage is good, the number of H_r retrievals can be improved by 3–4 times, thus the temporal resolution is improved. For example, for AT01 we obtained about 950 H_r estimates per day. Probably due to wave conditions, SNR data from higher elevation angles for ELLY was of poor quality for the year 2021. In total 180 days of data from DOY 1 of 2022 were used in this elevation angle range experiment.

The GNSS-IR tropospheric error is elevation dependent and higher elevation angle observations are less affected. The GNSS-IR tropospheric error is proportional to the reflector height. NYA2 has a reflector height $H_r \approx$ 48 m. In Fig. 8 we can see that applying strategy-e (No troposphere correction) leads to a very large elevation-dependent error. The H_r from low elevation angle data are negatively biased to higher elevation angle results by up to 2 m for NYA2. More importantly, applying strategy-f (Bending + MPF) is creating an elevation-dependent bias but in reversed direction. The H_r estimated from low elevation angle data are larger than higher elevation angle results, with similar magnitudes. On the other hand, strategy-b (MPF model), strategy-d (NITE model), and the bending corrections (strategy-a and -c) all seem to successfully remove the elevation angle dependence.

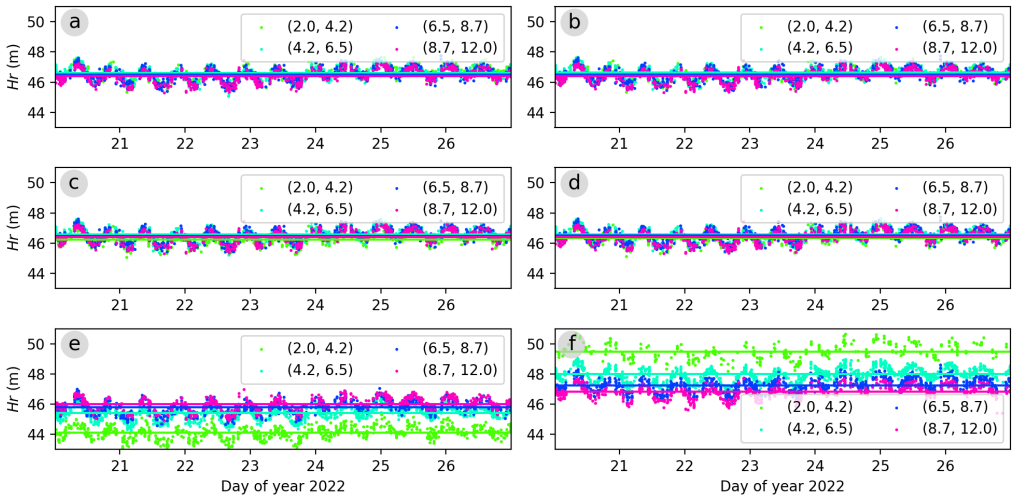

Figure 8: Seven-day reflector height time series of NYA2 using data at different elevation angle ranges (in different colors), with six different tropospheric error correction strategies: (a) Bending Bennett, (b) MPF, (c) Bending Ulich, (d) NITE, (e) No troposphere, (f) Bending + MPF.

Fig. 9 summarizes the elevation range cutting experiment for all 4 sites with data from the first 180 days of 2022. The average H_r retrieved with data from different elevation angle ranges together with 1 σ error are plotted as a function of elevation angle range. The 1 σ error was obtained by first fitting a smooth B-spline trend of H_r and then solving the standard deviation of the detrended residuals series. The results from strategy-e (No troposphere) and strategy-f (Bending + MPF) almost lie symmetric below and above the other results. Indeed we can see from Fig. 9 that the bending correction and the MPF model give corrections very close to each other. The "Bending + MPF" is almost like applying the bending correction (or MPF delay) twice. The tropospheric error affects the H_r nonlinearly so the symmetric pattern in Fig. 9 has a magnitude difference. For OSOU with H_r of only 3.7 m and AT01 with $H_r \approx 13$ m, we can see some strange elevation angle dependence at high elevation angles (above 12°). For such high elevation angles, tropospheric errors are quite small. The tropospheric error is an important contributor to the elevation angle dependent error, but not the only one. Other factors like wave height (Wang et al., 2021b) and antenna phase center (Dach et al., 2015) are also elevation-dependent. The fact that the results from a higher elevation angle range have larger σ also indicates that other errors exist.

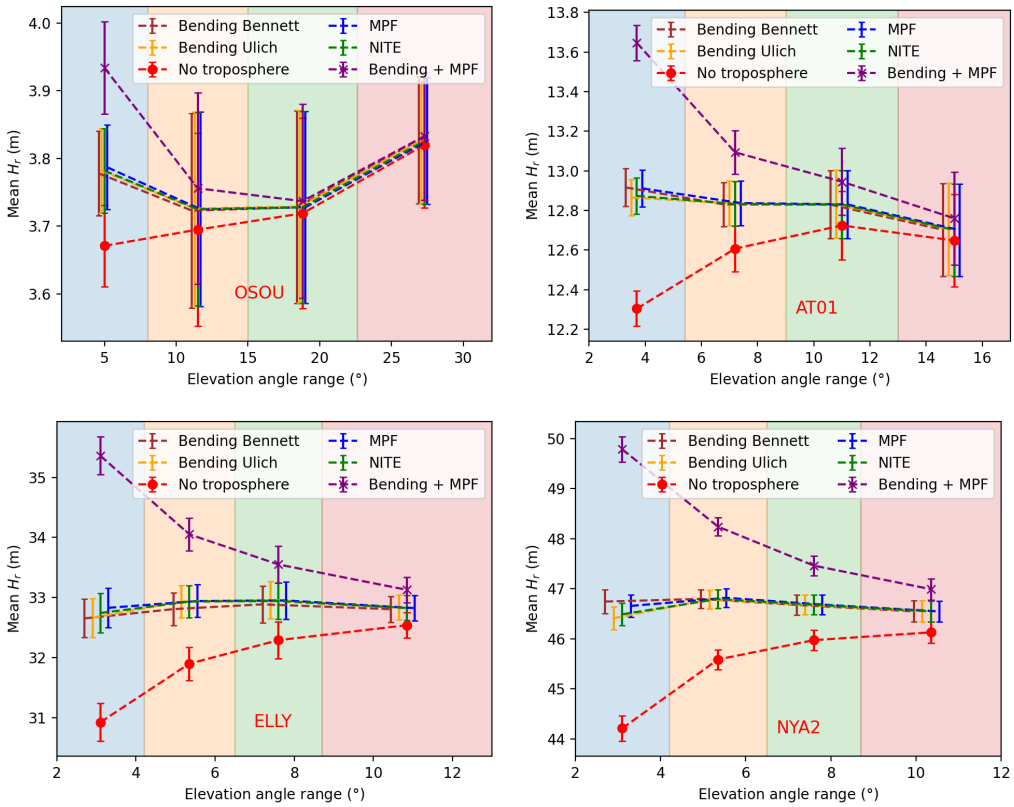

Figure 9: 180-day mean H_r and 1 σ errorbar from GNSS data at different elevation angle ranges (indicated by the colored background), for 4 sites from DOY 1 to 180 of 2022. The error bars are shifted in the x-axis direction to avoid overlapping. Notice that each subFigure has different x- and y-axis ranges.

Thus we are careful not to interpret results at the centimeter level here. The GNSS-IR tropospheric error is also almost linearly proportional to H_r. For stations located higher above sea level, like NYA2 and ELLY, the bias from the "No troposphere" and "Bending + MPF" can reach 1–3 m, well above the level of uncertainty of this experiment.

The elevation angle range cutting experiment confirmed that applying a combination of the bending correction and the path delay correction is over-compensating for GNSS-IR tropospheric error. Applying no tropospheric correction is also introducing a large elevation-dependent error, as expected. The results correspond to the theory in Section 2 and simulation in Section 3,

as we showed that the tropospheric geometric error is a lot small than the path delay. In the raytracing simulation in Section 3, we also see that the bending correction, the MPF delay model, and the NITE model are providing similar total tropospheric corrections, with subtle differences. In this experiment, their differences are smaller than the noise level (1 σ). This is also due to other unattended error sources. Therefore, we can not differentiate between the bending correction, the MPF delay model, and the NITE model with this elevation range cutting experiment.

4.2. Comparison with tide gauge

We processed 1 year of GNSS data from 4 stations and compared the sea level results with corresponding results from nearby tide gauges. The elevation angle ranges were set to $2 \sim 6^{\circ}$ for ELLY, $2.5 \sim 6^{\circ}$ for NYA2, $2 \sim 8^{\circ}$ for OSOU and $2 \sim 7^{\circ}$ for SC02. The purpose was to obtain stable H_r solutions but also to maximally expose the impact of tropospheric errors for investigation. Unfortunately, it is still difficult to compare absolute sea level from GNSS-IR and tide gauges. Firstly because different geodetic datums of the GNSS and the tide gauge might introduce uncertainties. Secondly, we did not apply antenna phase center corrections for GNSS-IR as this option was not available yet in the *gnssrefl* software. Instead, the sea level from the tide gauges was subtracted from the GNSS-IR H_r results to create a zero-mean residual series. We compared the different tropospheric error models using only the random error evolution over time of the zero-mean residuals. We tested 4 of the previously used 6 analysis strategies. The "No troposphere" and "Bending + MPF" were not included.

Fig. 10 depicts the zero-mean residuals of GNSS-IR H_r using a nearby tide gauge as a reference for the ELLY station. One can see that the bending correction with Bennett equation (a) is creating a non-stationary residual series during this one-year period. The ELLY station is located on the west coast of North America. In the middle of the year it is the summer season in North America with higher amount of atmospheric water vapor than in the winter season. This proves that by neglecting water vapor effects the Bennett equation is introducing a seasonal error. Similar results are seen for NYA2 with $H_r \approx 48\ m$. The summer-winter bias is about 10 cm for NYA2 and ELLY. For OSOU with $H_r \approx 3.7$ m, this effect is barely visible.

The winter-summer differences in the results with the Bennett bending equation (a) become even more clear when using daily average residuals (red dots in Fig. 10). Visually we can see that the daily average residuals from the

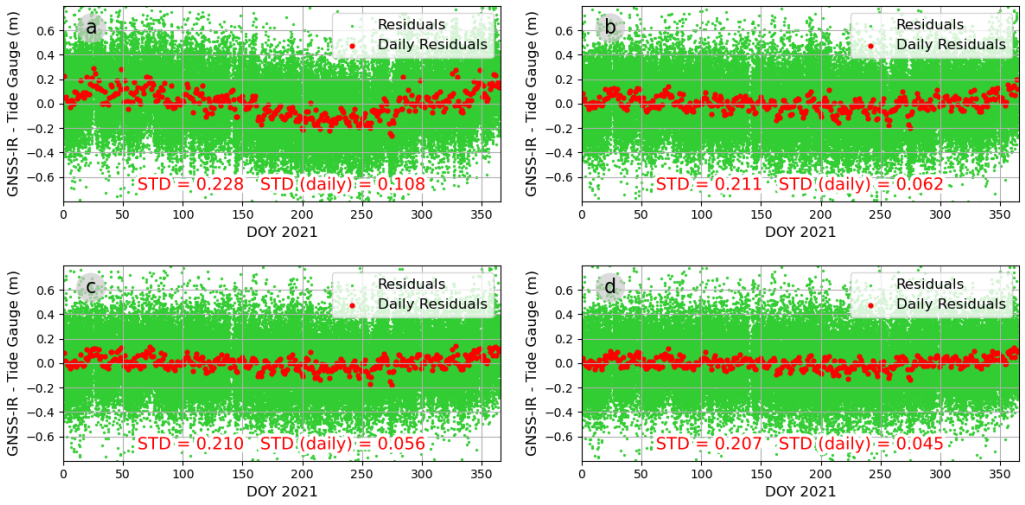

Figure 10: Residuals and daily average residuals at ELLY of GNSS-IR H_r retrievals using tide gauge as reference. (a) Bending Bennett, (b) MPF, (c) Bending Ulich, (d) NITE.

NITE model (d) are less scattered than the MPF delay model (b) and the bending correction with Ulich equation (c). This is confirmed by the standard deviation of the daily average residuals. The standard deviation of the daily average residuals of the NITE model (d) is 0.045 m, while it is 0.056 m for the Ulich bending model (c) and 0.062 m for the MPF delay model (b). Even though the original residual series ($\approx$ 200 values per day) have a similar level of standard deviation (0.211 m for the MPF model, 0.210 m for the Ulich bending model, and 0.207 m for the NITE model).

We used the Allan Deviation to further quantify the random error pattern of the residual series. The Allan Deviation σ_{ADEV} is defined as

$$\sigma^2_{ADEV}(\tau) = \frac{1}{2(M-1)} \sum_{i=1}^{M-1} [\overline{y_{i+1}} - \overline{y_i}]^2 \,, \tag{27}$$

where $\overline{y_i}$ is the ith fractional residual values averaged over the measurement interval, τ. The Allan Deviation is widely used to study signal stability over different time scales. The challenges to using the Allan Deviation to the GNSS-IR sea level residuals are the data gaps and non-uniform sampling time. For the 4 stations used we have very few data gaps. The residual series were linearly interpolated to generate uniform time series. For ELLY, with data from 2–6°, we obtained $\approx$ 200 H_r retrievals per day (1 every 7.5 min but

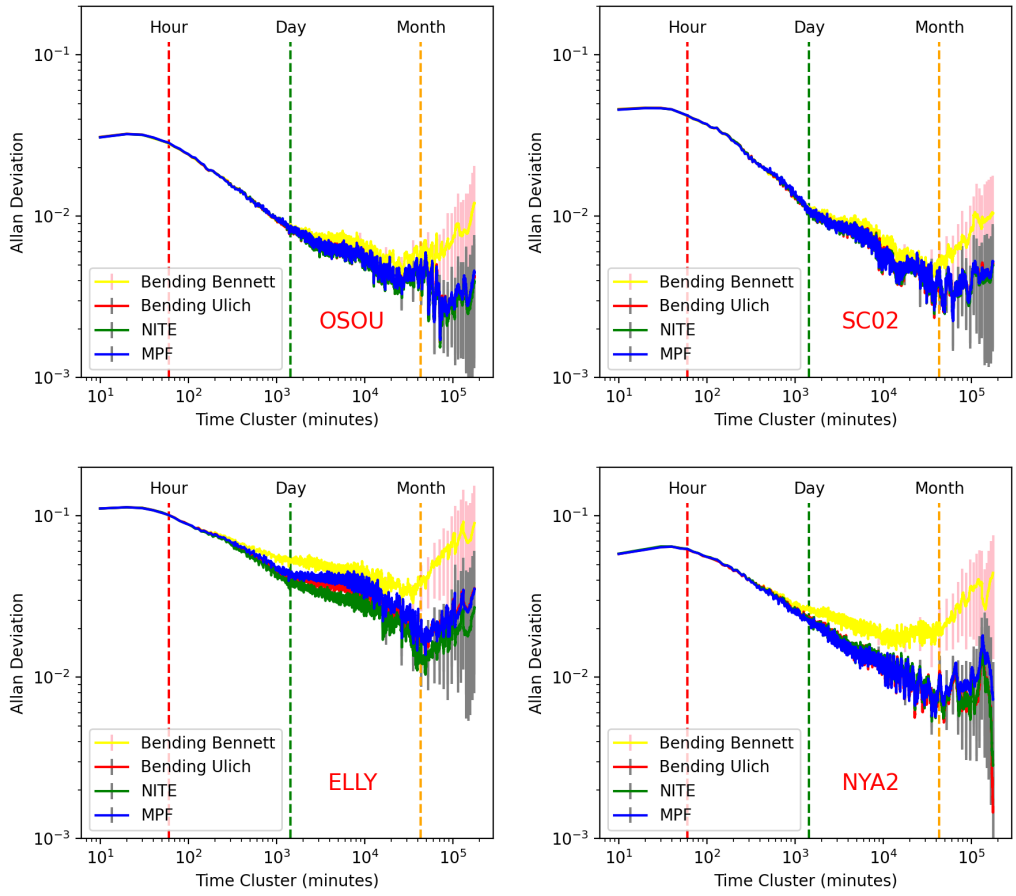

Figure 11: Allan Deviation of 1 year water level residuals for OSOU ($H_r \approx 3.7$ m), SC02 ($H_r \approx 5.5$ m) ELLY ($H_r \approx 33$ m) and NYA2 ($H_r \approx 48$ m).

unevenly sampled) and each SNR series contains $\approx$ 15 min of observations. Thus we used 10 min as the interpolation step.

The Allan Deviation σ-τ diagram for the 4 stations is presented in Fig. 11. Due to the fact that the residual series were interpolated to 10 min temporal resolution and the tide gauge data were also with about 10 min temporal resolution (1 min for OSOU, 6 min for SC02/ELLY and 10 min for NYA2), the σ_{ADEV} for τ <1 h may contain errors. Since we only have 1 year of data, the σ_{ADEV} with $\tau > 2$ months is also not reliable. From the results we can see that the Allan Deviation of all four models is the same for $\tau < 4$ h. For all 4 stations, the long-term trend caused by the Bennett equation is now clear.

The results from the Bennet bending correction (plotted yellow in Fig. 11) have a larger σ_{ADEV} for the time scale from a few hours to a few months, this corresponds to the variation of water vapor. Better long-term ($\tau > 4$ h) stability from the NITE model is observed at the ELLY station, but not the other three stations. This makes sense for the OSOU and SC02 station with $H_r < 10$ m where the reflection point is close to the antenna. NYA2 has a larger H_r than ELLY but the difference between the NITE model, MPF delay, and bending correction (with Ulich equation) is not noticeable. Comparing NYA2 and ELLY in Fig. 11, NYA2 also has a smaller σ_{ADEV}. This might be caused by differences in the local atmospheric conditions. NYA2 lies very north in the Arctic region (latitude $\approx 78.9°$) while ELLY is located on an oil platform at North America's west coast.

From this analysis, we conclude that the bending correction with the Bennett equation should not be used in GNSS-IR analysis, as it introduces long-term (from a few hours to half a year) errors in the sea-level retrievals. The NITE model seems to outperform the other models in some cases but more experiments are needed to draw a firm conclusion.

5. Discussion

We have deduced a rigorous tropospheric error model and validated this model using raytracing simulation and experiments with real data. Previously, Santamaría-Gómez and Watson (2017) proposed a bending correction and Williams and Nievinski (2017) used the direct mapping function delay model (MPF delay) for GNSS-IR tropospheric error corrections. From our raytracing simulation and experiment, we showed that numerically the bending correction and the MPF delay correction give very similar results to the rigorous NITE model. For the MPF delay, it is logical because the path delay is the dominating part in the NITE model (the first two terms in Eq. (22)). Physically, the MPF delay correction can also be interpreted as the "interferometric tropospheric path delay by neglecting the earth curvature effects and the small-angle mapping function difference". In this essence, the NITE model can be regarded as a more rigorous version of the MPF delay correction. When H_r is small and/or e_T is large, the difference between the two becomes negligible.

It is surprising that the bending correction (using the Ulich equation), which only uses the atmospheric bending angle, performs so close to the MPF delay and the NITE model. This can probably be explained by that

the atmospheric bending angle is highly correlated to the ground refractivity and the mapping function (Yan and Ping, 1995; Yan, 1998; Feng et al., 2022). In a series of works, Yan (1998) demonstrated that the atmospheric bending angle can be modeled as $\Delta e = N_0\, mpf\, \cos e_T$, with mpf being the commonly used mapping function. With the help of this relation (3rd line in Eq. (28)), we can rewrite the bending correction by Eq. (25) as

$$\begin{aligned}\tau_i &= 2H_r \sin e_A \\ &= 2H_r(\sin e_T \cos \Delta e + \sin \Delta e \cos e_T) \\ &\approx 2H_r \sin e_T + 2H_r \Delta e \cos e_T \\ &= 2H_r \sin e_T + 2H_r N_0\, \overline{mpf}\, \cos e_T\,. \end{aligned} \tag{28}$$

At low elevation angles $\cos e_T \approx 1$, thus the bending correction becomes the MPF delay given by Eq. (26). We emphasize that the bending correction is theoretically problematic. In the zenith direction, $\cos e_T = 0$ and the bending correction is 0, which violates the facts. Both the atmosphere and bending correction are continuous, a violation at $e_T = 90°$ means that the bending correction is incorrect for all high elevation angles. We have observed this effect in the raytracing simulation (low-right part in Fig. 4). In the experiment in Section 4.1, for the higher elevation data in OSOU, we also see that the MPF and NITE models give almost the same results but the results from the bending correction are slightly different.

With Eq. (28) we provide theoretical justification to the bending correction but it is necessary to adopt a better equation to calculate the bending angle, like the Ulich (1981) equation. In Fig. 12 we plotted the bending angle model error of the Bennett and Ulich equations (model value minus raytracing) w.r.t. the zenith wet delay (ZWD) for all the 14 radiosonde stations. The Ulich equation performs better and is more consistent in different ZWD situations. Experimental results presented in Section 4.2 showed the time-varying error introduced by the Bennett equation. The water vapor contents are also location dependent thus the Bennett equation will also introduce different errors in different places.

The $\overline{mpf}$ in Eq. (28) has an average symbol because we are using the Ulich equation in the experiments which implicitly contains a mapping function (elevation angle dependence) but is fixed over time and location (averaged). Comparing the results from the (b) MPF and (c) Bending Ulich in Section 4.2, the bending correction performs not worse than the MPF delay in the time domain random errors. This indicates that the GNSS-IR results

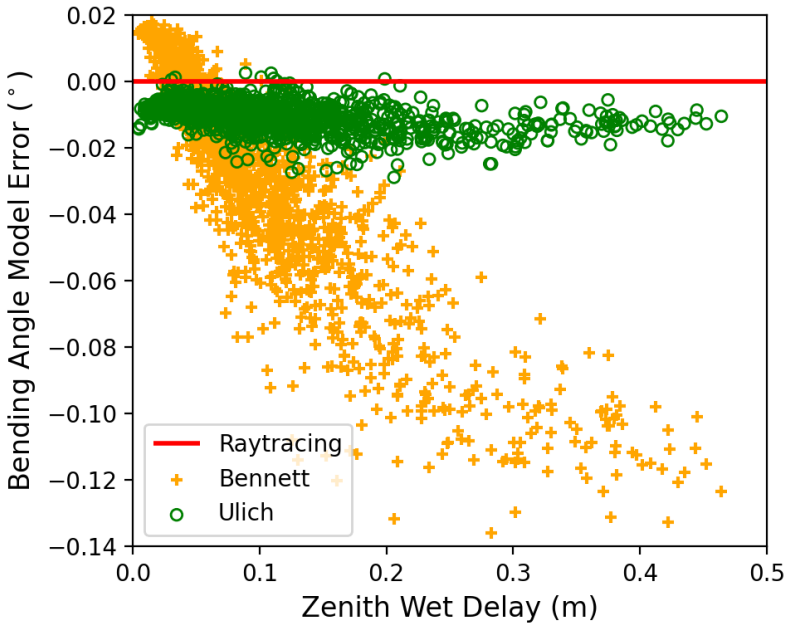

Figure 12: Bending angle model errors over zenith wet delay at $e_T = 2°$ for 14 globally distributed radiosonde stations.

are not very sensitive to the variation of the mapping function over time in the MPF delay correction. This corresponds to our discussion about the bias and random error of the total delay in Section 3.2, where we showed that the error in the mapping function is mainly introducing a bias to the NITE model.

With the experiments we rule out three tropospheric error correction strategies, the "No Troposphere", the "Bending + MPF" and the bending correction with the Bennett equation. The bending correction with the Ulich equation, the MPF delay model and the NITE model overall perform closely in the essence of random errors. The bending correction (with Ulich equation), though not theoretically strict, is very convenient to apply for SNR-based GNSS-IR application. The MPF delay model is more complicated to apply than the bending correction and performs similarly at low elevation angles, but at higher elevation angles it performs better. The NITE model proposed in this work is more complicated than the MPF model and the bending correction but it is more rigorous, e.g. concerning the earth curvature effects. In Section 4.2 we only compared the random error perfor-

mance but not the bias. One reason is that both the bending correction and the MPF delay model assume a flat reflective surface. In the NITE model, the earth curvature effects (magnitudes in Table 2) are tightly integrated. At NYA2 with $H_r \approx 48$ m, with data from $2.5 \sim 6°$, the 1-year average H_r for the bending correction is 46.605 m, 46.647 m for the MPF delay model and 46.616 m for the NITE model.

Data from higher elevation angles are less impacted by the tropospheric error, but at many locations, due to the surrounding environment, high elevation data are not available for GNSS-IR applications. Data from high elevation angles are also more sensitive to ocean roughness (Purnell et al., 2020; Wang et al., 2021b). In Fig. 9 we can see that the error bar of H_r using high elevation angle data is usually larger than that from the low elevation data. This is caused by the GNSS antenna gain pattern. Interferometric fringes are cleaner at low elevation angles. The closer the antenna is to the ocean surface, the smaller the tropospheric error. On the other hand, an antenna located higher, observes more interferometric cycles and thus the temporal resolution is improved. Besides, in places where tidal changes are large (Garrett, 1972), it is impossible to continuously have a GNSS antenna very close to the ocean surface. The NITE tropospheric error model described in this work performs better in those challenging situations. Thus, the application of GNSS-IR sea-level monitoring is expanded.

6. Conclusion

We deduced a tropospheric error model for GNSS-IR. The model takes into account earth curvature effects and the small-angle mapping function difference. This model contains two parts, a straight-line geometric error and a path delay. The geometric error is derived using the specular reflection with curved signal path and curved earth surface. The path delay is derived following the definition of the mapping function. We call this GNSS-IR tropospheric error model the NITE (New Interferometric Tropospheric Error) model.

We validated the NITE model using raytracing with radiosonde atmosphere profiles, together with two previously proposed models, the bending correction and the MPF delay. We found that, numerically, the geometric part of GNSS-IR tropospheric error is a lot smaller than the path delay. For a 20 m antenna, the geometric part is less than 5 % of the delay part at 2°and even smaller at higher elevation angles. The NITE model outperforms previ-

ous models in both sub-components and total tropospheric error. We found that the inaccuracy in mapping function products is introducing a systematic bias to the NITE model total tropospheric error and the random error is limited by the representativeness of the average layer refractivity.

We tested six tropospheric error correction strategies with two sets of experiments. Three of them, the "No troposphere", "Bending + MPF delay" and the "Bending with Bennett equation" are ruled out using elevation dependence and season trend criterion. The NITE model seems to outperform other models in one station but more experiments will be needed to draw a conclusion. Finally, we discussed the link between the bending correction, the MPF delay, and the NITE model. We showed that at low elevation angles the bending correction and the MPF delay are more equivalent to each other, not complementary.

A major approximation of the NITE model is that we only considered the vertical distribution of the atmosphere, while in GNSS positioning it is widely accepted that the horizontal structure of the atmosphere has an impact on signal propagation (Elgered et al., 2019). In the future, we should consider applying a similar concept to GNSS-IR. We tested the NITE model with experiments using the SNR-based GNSS-IR. The phase-based GNSS-IR, though more complicated and less robust, can reach higher accuracy and temporal resolution. Experiments with phase-based GNSS-IR can be used to assess the NITE model in a different way.

Acknowledgement

This research is supported by a grant from the Hasselblad Foundation. The geodetic research infrastructure at the Onsala site is supported by the Swedish Mapping, Cadastral and Land Registration Authority. The traditional tide gauge is operated in collaboration with the Swedish Meteorological and Hydrological Institute.

Data Statement

The radiosonde data used in this study were obtained from NOAA Integrated Global Radiosonde Archive (www.ncei.noaa.gov/products/weather-balloon/). The Vienna mapping function products and code were obtained from VMF Data Server (https://vmf.geo.tuwien.ac.at/). High-rate GNSS data for SC02, AT01 and ELLY were downloaded from UNVACO, together

with the meteorology rinex files for ELLY. Meteorology data from AT01 and SC02 were obtained from Iowa State University Iowa Environmental Mesonet (https://mesonet.agron.iastate.edu/). GNSS data for NYA2 was available from the IGS server hosted by CDDIS. Meteorology data from NYA2 were obtained from Geodetic Earth Observatory, Ny-Ålesund. Tide gauge data near ELLY and SC02 were obtained from NOAA's Center for Operational Oceanographic Products and Services (CO-OPS). Tide gauge data for NYA2 were obtained from "Se havnivå" of the Norwegian Mapping Authority. GNSS, meteorology, and tide gauge at OSOU were collected by Onsala Space Observatory and are available by contacting the author.

Declaration of Competing Interest

The authors declare that they have no known competing financial interests or personal relationships that could have appeared to influence the work reported in this paper.

Appendix A. A two-step 2D raytracing for GNSS-IR

To validate the interferometric tropospheric error model, we need to carry out raytracing for both the direct and reflected signal. Raytracing for direct GNSS signals has been well studied in space geodesy (Hobiger et al., 2008; Nafisi et al., 2012). Here we adapt a 2D raytracing tool we develop and validated in a previous study (Feng et al., 2020) to do the raytracing for the reflected signal. This direct 2D raytracing is very similar to what was used to generate the Vienna Mapping Function (Boehm and Schuh, 2003). With a given refractivity profile, the direct raytracing algorithm starts with an initial apparent elevation angle and calculates the signal path layer by layer. Usually, it was regarded that assuming an infinite satellite distance will cause a negligible error for GNSS. So the raytracing iteration stops when the out-going elevation angle at the top of the atmosphere is close enough to the true elevation angle (Boehm and Schuh, 2003). A major change we made here is that the true elevation angle instead of the "out-going" elevation angle is used. The true elevation angle is calculated by extending a straight ray from the top of the atmosphere to the satellite assuming a 20,000 km GNSS orbit height. Numerically it only makes a very small difference but it is theoretically more rigorous. In this way, the geometric signal path for the direct and reflected signal can be clearly defined.

We simplified the raytracing for the reflected signal using the specular reflection assumption. Firstly, since we are using a layered atmosphere, the reflected signal is symmetric at two sides of the reflection point below the antenna. Secondly, we used a spherical approximation for earth instead of an ellipsoid.

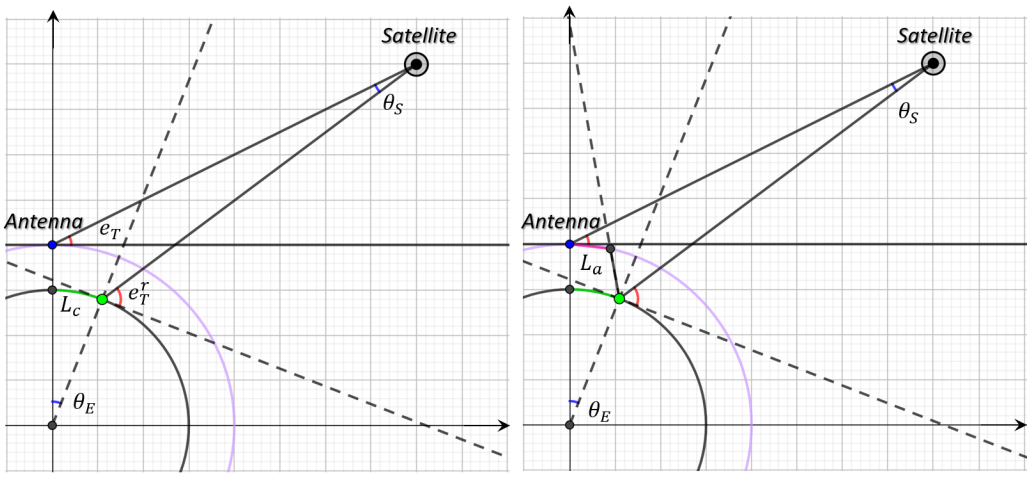

Figure A.13: Demonstration of step 2 and 3 of the reflected signal raytracing

The procedures of raytracing are:

1. Direct signal raytracing at the antenna with a given true elevation angle. The direct signal path is obtained. The satellite coordinate in the earth-centered 2D Cartesian coordinate system is calculated using the true elevation angle and GNSS orbit radius.
2. Calculate the true elevation angle for the reflected signal e_T^r with a priori L_c, where L_c is the curvature distance from the reflection point to the projection of the antenna on the big circle of the sea surface. With an initial L_c, the coordinate of the refraction point, the earth center angle θ_E, and the satellite angle θ_S can be analytically calculated. The true elevation angle e_T^r for the reflected signal is obtained for this given L_c.
3. Raytracing the down-leg path of the reflected signal using e_T^r and the refractivity profile down to the ocean surface. Mirror the down-leg signal over the perpendicular line at the reflection point, the up-leg path is obtained. The up-leg ray will intersect with the earth-centered circle crossing the GNSS antenna, with a curvature distance L_a. By comparing

this intersection point and the positioning of the GNSS antenna in this circle, we know L_c is too large or too small. Iterate until the up-leg ray intersects the circle with a distance < 0.1 mm to the antenna. Since the reflector height is 100 m at maximum, the circle through the antenna and the circle through the ocean surface are close to parallel locally. Iteration of L_c is done by subtracting L_a (can be negative) from L_c.

4. Calculate interferometric delay and tropospheric error by definition using the direct and reflected signal path.

References

Bennett, G.G., 1982. The Calculation of Astronomical Refraction in Marine Navigation. Journal of Navigation 35, 255–259. doi:10.1017/S0373463300022037.

Bevis, M., Businger, S., Herring, T.A., Rocken, C., Anthes, R.A., Ware, R.H., 1992. GPS meteorology: remote sensing of atmospheric water vapor using the global positioning system. Journal of Geophysical Research 97, 15787. doi:10.1029/92jd01517.

Boehm, J., Schuh, H., 2003. Vienna Mapping Functions, in: Proceedings of the 16th Working Meeting on European VLBI for Geodesy and Astrometry, May 9-10, 2003, Leipzig, Germany. pp. 131–143.

Boehm, J., Werl, B., Schuh, H., 2006. Troposphere mapping functions for GPS and very long baseline interferometry from European Centre for Medium-Range Weather Forecasts operational analysis data. Journal of Geophysical Research: Solid Earth 111, 1–9. doi:10.1029/2005JB003629.

Boisits, J., Landskron, D., Böhm, J., 2020. VMF3o: the Vienna Mapping Functions for optical frequencies. Journal of Geodesy 94, 1–11. doi:10.1007/S00190-020-01385-5/TABLES/8.

Dach, R., Simon, L., Peter, W., Pierre, F., 2015. Bernese GNSS Software Version 5.2. November, University of Bern, Bern Open Publishing, Bern, Switzerland. doi:10.7892/boris.72297.

Dao, D., Rizos, C., Wang, J., 2002. Location-based services: technical and business issues. GPS Solutions 2002 6:3 6, 169–178. doi:10.1007/S10291-002-0031-5.

Davis, J.L., Elgered, G., Niell, A.E., Kuehn, C.E., 1993. Ground-based measurement of gradients in the "wet" radio refractivity of air. Radio Science 28, 1003–1018. doi:10.1029/93RS01917.

Duan, J., Bevis, M., Fang, P., Bock, Y., Chiswell, S., Businger, S., Rocken, C., Solheim, F., van Hove, T., Ware, R., McClusky, S., Herring, T.A., King, R.W., 2002. GPS Meteorology: Direct Estimation of the Absolute Value of Precipitable Water. doi:10.1175/1520-0450(1996)035¡0830:gmdeot¿2.0.co;2.

Durre, I., Vose, R.S., Wuertz, D.B., 2006. Overview of the integrated global radiosonde archive. Journal of Climate 19, 53–68. doi:10.1175/JCLI3594.1.

Elgered, G., Johansson, J.M., Rönnäng, B.O., Davis, J.L., 1997. Measuring regional atmospheric water vapor using the Swedish permanent GPS network. Geophysical Research Letters 24, 2663–2666. doi:10.1029/97GL02798.

Elgered, G., Ning, T., Forkman, P., Haas, R., 2019. On the information content in linear horizontal delay gradients estimated from space geodesy observations. Atmospheric Measurement Techniques 12, 3805–3823. doi:10.5194/amt-12-3805-2019.

Fabra, F., Cardellach, E., Rius, A., Ribó, S., Oliveras, S., Nogués-Correig, O., Belmonte Rivas, M., Semmling, M., D'Addio, S., 2012. Phase altimetry with dual polarization GNSS-R over sea ice. IEEE Transactions on Geoscience and Remote Sensing 50, 2112–2121. doi:10.1109/TGRS.2011.2172797.

Feng, P., Haas, R., Elgered, G., Strandberg, J., 2022. Calibrating tropospheric errors on ground-based GNSS reflectometry: calculation of bending and delay effects. EGU22 doi:10.5194/EGUSPHERE-EGU22-12698.

Feng, P., Li, F., Yan, J., Zhang, F., Barriot, J.P., 2020. Assessment of the accuracy of the saastamoinen model and vmf1/vmf3 mapping functions with respect to ray-tracing from radiosonde data in the framework of gnss meteorology. Remote Sensing 12, 1–21. doi:10.3390/rs12203337.

Fleming, E.L., Chandra, S., Barnett, J.J., Corney, M., 1990. Zonal mean temperature, pressure, zonal wind and geopotential height as functions of latitude. Advances in Space Research doi:10.1016/0273-1177(90)90386-E.

Garrett, C., 1972. Tidal Resonance in the Bay of Fundy and Gulf of Maine. Nature 1972 238:5365 238, 441–443. URL: https://www.nature.com/articles/238441a0, doi:10.1038/238441a0.

Georgiadou, Y., Kleusberg, A., 1988. On carrier signal multipath effects in relative GPS positioning. Manuscripta geodaetica 13, 172–179.

Geremia-Nievinski, F., Hobiger, T., Haas, R., Liu, W., Strandberg, J., Tabibi, S., Vey, S., Wickert, J., Williams, S., 2020a. SNR-based GNSS reflectometry for coastal sea-level altimetry: results from the first IAG inter-comparison campaign. Journal of Geodesy 94. URL: https://doi.org/10.1007/s00190-020-01387-3.

Geremia-Nievinski, F., Makrakis, M., Tabibi, S., 2020b. Inventory of published GNSS-R stations, with focus on ocean as target and SNR as observable. URL: https://zenodo.org/record/3668360, doi:10.5281/ZENODO.3668360.

Gravalon, T., Seoane, L., Ramillien, G., Darrozes, J., Roblou, L., 2022. Determination of weather-induced short-term sea level variations by GNSS reflectometry. Remote Sensing of Environment 279, 113090. doi:10.1016/J.RSE.2022.113090.

Herring, T.A., King, R.W., Floyd, M.A., McClusky, S.C., 2010. GAMIT Reference Manual: GPS Analysis at MIT, Release 10.6. June, Massachusetts Institute of Technology, Cambridge, MA, USA.

Hobiger, T., Ichikawa, R., Takasu, T., Koyama, Y., Kondo, T., 2008. Ray-traced troposphere slant delays for precise point positioning. Earth, Planets and Space 60, 1–4. doi:10.1186/bf03352809.

JPL, . PPPX. URL: https://pppx.gdgps.net/.

Kwok, S., 2017. A Spherical Earth, in: Our Place in the Universe. Springer, Cham, pp. 33–48. doi:10.1007/978-3-319-54172-3_5.

Lagler, K., Schindelegger, M., Böhm, J., Krásná, H., Nilsson, T., 2013. GPT2: Empirical slant delay model for radio space geodetic techniques. Geophysical Research Letters 40, 1069–1073. doi:10.1002/grl.50288.

Landskron, D., 2017. Modeling tropospheric delays for space geodetic techniques. Ph.D. thesis. Vienna University of Technology.

Landskron, D., Böhm, J., 2018. VMF3/GPT3: refined discrete and empirical troposphere mapping functions. Journal of Geodesy 92, 349–360. doi:10.1007/s00190-017-1066-2.

Larson, K.M., 2019. Unanticipated uses of the global positioning system. Annual Review of Earth and Planetary Sciences 47, 19–40. doi:10.1146/annurev-earth-053018-060203.

Larson, K.M., Löfgren, J.S., Haas, R., 2013a. Coastal sea level measurements using a single geodetic GPS receiver. Advances in Space Research 51, 1301–1310. doi:10.1016/J.ASR.2012.04.017.

Larson, K.M., Ray, R.D., Nievinski, F.G., Freymueller, J.T., 2013b. The accidental tide gauge: A GPS reflection case study from kachemak bay, Alaska. IEEE Geoscience and Remote Sensing Letters 10, 1200–1204. URL: `http://ieeexplore.ieee.org.`, doi:10.1109/LGRS.2012.2236075.

Larson, K.M., Small, E.E., Gutmann, E.D., Bilich, A.L., Braun, J.J., Zavorotny, V.U., Larson, C.., Small, E.E., Gutmann, E.D., Bilich, A.L., Braun, J.J., Zavorotny, V.U., 2008. Use of GPS receivers as a soil moisture network for water cycle studies. Geophysical Research Letters 35. doi:10.1029/2008GL036013.

Löfgren, J.S., Haas, R., 2014. Sea level measurements using multi-frequency GPS and GLONASS observations. Eurasip Journal on Advances in Signal Processing 2014, 1–13. doi:10.1186/1687-6180-2014-50/FIGURES/8.

Meeks, M., 1976. 2.5. Refraction Effects in the Neutral Atmosphere. Methods in Experimental Physics 12, 186–200. doi:10.1016/S0076-695X(08)60686-9.

Minzner, R., Reber, C., Jacchia, L., Huang, F., Cole, A., Kantor, A., Kenesbea, T., Zimmerman, S., Forbes, J., 1976. Defining Constants, Equations, and Abbreviated Tables of the 1975 U.S. Standard Atmosphere. NASA Technical Report R-459.

Möller, G., Landskron, D., 2019. Atmospheric bending effects in GNSS tomography. Atmospheric Measurement Techniques 12, 23–34. doi:10.5194/amt-12-23-2019.

Nafisi, V., Urquhart, L., Santos, M.C., Nievinski, F.G., Böhm, J., Wijaya, D.D., Schuh, H., Ardalan, A.A., Hobiger, T., Ichikawa, R., Zus, F., Wickert, J., Gegout, P., 2012. Comparison of ray-tracing packages for troposphere delays. IEEE Transactions on Geoscience and Remote Sensing 50, 469–481. doi:10.1109/TGRS.2011.2160952.

Niell, A.E., 1996. Global mapping functions for the atmosphere delay at radio wavelengths. Journal of Geophysical Research: Solid Earth 101, 3227–3246. doi:10.1029/95JB03048.

Nikolaidou, T., Santos, M.C., Williams, S.D., Geremia-Nievinski, F., 2020. Raytracing atmospheric delays in ground-based GNSS reflectometry. Journal of Geodesy 94, 1–12. doi:10.1007/s00190-020-01390-8.

Park, K.D., Nerem, R.S., Schenewerk, M.S., Davis, J.L., 2004. Site-specific multipath characteristics of global IGS and CORS GPS sites. Journal of Geodesy 77, 799–803. doi:10.1007/s00190-003-0359-9.

Peng, D., Hill, E.M., Li, L., Switzer, A.D., Larson, K.M., 2019. Application of GNSS interferometric reflectometry for detecting storm surges. GPS Solutions 23, 1–11. doi:10.1007/s10291-019-0838-y.

Pham, N.D., 2011. The Economic Benefits of Commercial GPS Use in the U.S. and the Costs of Potential Disruption. ERN: Technology (Topic) .

Ping, J., Yan, H., Wang, G., Qian, Z., Zhou, R., Shu, F., 1997. A comparison of different tropospheric mapping functions by elevation cut-off tests. Monthly Notices of the Royal Astronomical Society 287, 812–816. URL: https://academic.oup.com/mnras/article/287/4/812/983064, doi:10.1093/MNRAS/287.4.812.

Purnell, D., Gomez, N., Chan, N.H., Strandberg, J., Holland, D.M., Hobiger, T., 2020. Quantifying the Uncertainty in Ground-Based GNSS-Reflectometry Sea Level Measurements. IEEE Journal of Selected Topics in Applied Earth Observations and Remote Sensing 13, 4419–4428. doi:10.1109/JSTARS.2020.3010413.

re3data.org, . VMF Data Server. URL: https://vmf.geo.tuwien.ac.at/, doi:10.17616/R3RD2H.

Roesler, C., Larson, K.M., 2018. Software tools for GNSS interferometric reflectometry (GNSS-IR). GPS Solutions 22, 1–10. URL: http://dx.doi.org/10.1007/s10291-018-0744-8, doi:10.1007/s10291-018-0744-8.

Roussel, N., Ramillien, G., Frappart, F., Darrozes, J., Gay, A., Biancale, R., Striebig, N., Hanquiez, V., Bertin, X., Allain, D., 2015. Sea level monitoring and sea state estimate using a single geodetic receiver. Remote Sensing of Environment 171, 261–277. doi:10.1016/J.RSE.2015.10.011.

Rüeger, J.M., 2002. Refractive Index Formulae for Radio Waves, in: FIG Technical Program, FIG XXII International Congress, Washington, D.C. USA. pp. 1–13.

Saastamoinen, J., 1973. Contributions to the theory of atmospheric refraction - Part II. Refraction corrections in satellite geodesy. Bulletin Géodésique 47, 428. doi:10.1038/130428b0.

Santamaría-Gómez, A., Watson, C., 2017. Remote leveling of tide gauges using GNSS reflectometry: case study at Spring Bay, Australia. GPS Solutions 21, 451–459. doi:10.1007/s10291-016-0537-x.

Semmling, A.M., Schmidt, T., Wickert, J., Schn, S., Fabra, F., Cardellach, E., Rius, A., 2012. On the retrieval of the specular reflection in GNSS carrier observations for ocean altimetry. Radio Science 47, 1–13. doi:10.1029/2012RS005007.

Sokolovskiy, S., Kuo, Y.H., Rocken, C., Schreiner, W.S., Hunt, D., Anthes, R.A., 2006. Monitoring the atmospheric boundary layer by GPS radio occultation signals recorded in the open-loop mode. Geophysical Research Letters 33, 12–15. doi:10.1029/2006GL025955.

Stone, R.C., 1996. An Accurate Method for Computing Atmospheric Refraction. Publications of the Astronomical Society of the Pacific 108, 1051. doi:10.1086/133831.

Strandberg, J., 2020. New methods and applications for interferometric GNSS reflectometry (Ph.D. thesis). Ph.D. thesis. Chalmers Univsesity of Technology.

Tabibi, S., Geremia-Nievinski, F., Francis, O., van Dam, T., 2020. Tidal analysis of GNSS reflectometry applied for coastal sea level sensing in Antarctica and Greenland. Remote Sensing of Environment 248, 111959. doi:10.1016/j.rse.2020.111959.

Treuhaft, R.N., Lowe, S.T., Zuffada, C., Chao, Y., 2001. 2-cm GPS altimetry over Crater lake. Geophysical Research Letters 28, 4343–4346. doi:10.1029/2001GL013815.

Ulich, B.L., 1981. Millimeter wave radio telescopes: Gain and pointing characteristics. International Journal of Infrared and Millimeter Waves 2, 293–310. doi:10.1007/BF01007036.

Wang, N., Xu, T., Gao, F., He, Y., Meng, X., Jing, L., Ning, B., 2022. Sea-level monitoring and ocean tide analysis based on multipath reflectometry using received strength indicator data from multi-GNSS signals. IEEE Transactions on Geoscience and Remote Sensing , 1–1doi:10.1109/TGRS.2022.3219074.

Wang, X., He, X., Xiao, R., Song, M., Jia, D., 2021a. Millimeter to centimeter scale precision water-level monitoring using GNSS reflectometry: Application to the South-to-North Water Diversion Project, China. Remote Sensing of Environment 265, 112645. doi:10.1016/j.rse.2021.112645.

Wang, X., He, X., Zhang, Q., 2019. Evaluation and combination of quad-constellation multi-GNSS multipath reflectometry applied to sea level retrieval. Remote Sensing of Environment 231, 111229. doi:10.1016/j.rse.2019.111229.

Wang, Y., Breitsch, B., Morton, Y.T., 2021b. A State-Based Method to Simultaneously Reduce Cycle Slips and Noise in Coherent GNSS-R Phase Measurements from Open-Loop Tracking. IEEE Transactions on Geoscience and Remote Sensing 59, 8873–8884. doi:10.1109/TGRS.2020.3036031.

Williams, S.D., Nievinski, F.G., 2017. Tropospheric delays in ground-based GNSS multipath reflectometry—Experimental evidence from coastal sites. Journal of Geophysical Research: Solid Earth 122, 2310–2327. doi:10.1002/2016JB013612.

Xie, S., 2022. Continuous measurement of sea ice freeboard with tide gauges and GNSS interferometric reflectometry. Remote Sensing of Environment 280, 113165. doi:10.1016/J.RSE.2022.113165.

Yan, H., 1998. New continued fraction form of the mapping functions of atmospheric refraction corrections. Astronomical & Astrophysical Transactions 16, 61–73. doi:10.1080/10556799808208145.

Yan, H., Ping, J., 1995. The Generator Function Method of the Tropospheric Refraction Corrections. The Astronomical Journal 110, 934. doi:10.1086/117574.

Yan, H., Zhang, G., Guo, P., Hong, Z., 2002. Discussion and comparison of the mapping functions in radio frequencies. Terrestrial, Atmospheric and Oceanic Sciences 13, 563–575. doi:10.3319/TAO.2002.13.4.563(A).

Ye, M., Jin, S., Jia, Y., 2022. Ten-Minute Sea-Level Variations From Combined Multi-GNSS Multipath Reflectometry Based on a Weighted Iterative Least-Square Method. IEEE Transactions on Geoscience and Remote Sensing 60, 1–10. doi:10.1109/TGRS.2022.3194033.

Zus, F., Dick, G., Dousa, J., Wickert, J., 2015. Systematic errors of mapping functions which are based on the VMF1 concept. GPS Solutions 19, 277–286. doi:10.1007/s10291-014-0386-4.